ADVANCED MATERIALS

Supporting Information

for *Adv. Mater.,* DOI: 10.1002/adma.202100381

Complex Metal Nanostructures with Programmable Shapes from Simple DNA Building Blocks

*Jingjing Ye, Olha Aftenieva, Türkan Bayrak, Archa Jain, Tobias A. F. König, Artur Erbe, and Ralf Seidel**

Complex metal nanostructures with programmable shapes from simple DNA building blocks

*Jingjing Ye, Olha Aftenieva, Türkan Bayrak, Archa Jain, Tobias A. F. König, Artur Erbe, Ralf Seidel**

Dr. Jingjing Ye, Prof. Dr. Ralf Seidel

Molecular Biophysics group, Peter Debye Institute for Soft Matter Physics, Universität Leipzig, 04103 Leipzig, Germany

Olha Aftenieva, Dr. habil. Tobias A. F. König

Leibniz-Institut für Polymerforschung Dresden e. V., Hohe Straße 6, 01069 Dresden, Germany

Dr. Türkan Bayrak, Archa Jain, Dr. Artur Erbe

Institute of Ion Beam Physics and Materials Research, Helmholtz-Zentrum Dresden-Rossendorf, 01328 Dresden, Germany

Dr. Jingjing Ye, Dr. Türkan Bayrak, Dr. habil. Tobias A. F. König, Dr. Artur Erbe, Prof. Dr. Ralf Seidel

Center for Advancing Electronics Dresden (cfaed), Technische Universität Dresden, Helmholtzstraße 18, 01069 Dresden, Germany

Archa Jain

Faculty of Electrical Engineering and Information Technology, Chair of Nanoelectronics Technologies, Technische Universität Chemnitz, 09107 Chemnitz, Germany

Email: ralf.seidel@physik.uni-leipzig.de

Note S1. Interface design for the docking of mold elements.

Interfaces that support specific interactions between the different elements were based on a previously established concept to linearly connect standard molds[1]. All applied elements shared the same interface geometry based on a 10x10 lattice of DNA helix ends[1]. The pattern of recessed and exposed helix ends in the outer two layers was for all structures identical (see Figure S1 below). It was taken from the design of the mold element, in which all DNA helices had the same length. This also provides that its two ends, which are called left (L) and right (R) end, are asymmetric. Interacting helix ends of the interface dock only "neat-less", i.e., gap-free, onto each other, if a left mold end docks onto a right mold end (see Figure S1b below). The helix ends of an interface were either interacting (Figure S1a) in an attractive (shown in yellow) or a repulsive manner (shown in blue). For attractive helix ends, the terminal staples were extended by two nucleotides (nt) with respect to the scaffold crossing either at their 5′-ends (accompanied with a corresponding recession of the 3′- ends) or at their 3' ends (accompanied with a corresponding recession of the 5′- ends). The sequence of the overhangs was chosen to allow hybridization with the scaffold section at the staple recessions. The repulsive helix ends had 6 nt single-stranded DNA (ssDNA) overhangs of the same sequence at both 5' and 3' ends. Changing the overhang type, the pattern of attractive vs. repulsive helix ends as well as the overhang sequence allows to establish different interfaces that are just specific to a particular complement[1,2]. Full interface designs for all employed structures of this work are given in Figures S23-31.

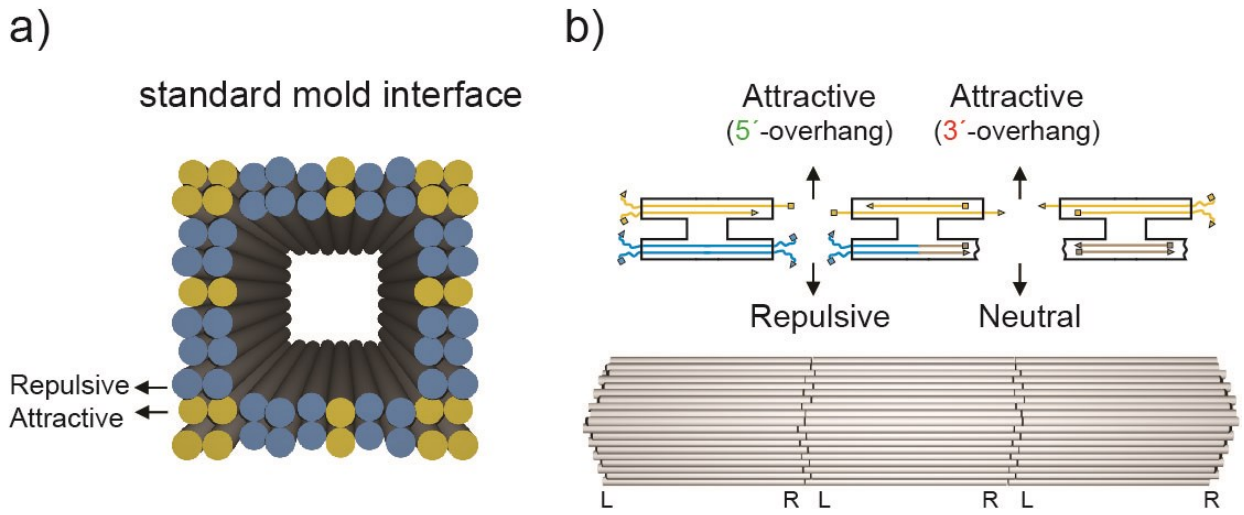

Figure S1. Interface design for the docking of mold elements.

(**a**) Standard mold interface design with attractive ends marked in yellow and repulsive ends marked in blue. (**b**) Linear docking of mold elements in which a right end (R) docks always onto a left (L) end in a neat-less manner (bottom). Attractive helix ends were established by extending the 5' staple overhangs and correspondingly recessing the 3' overhangs or vice versa using 5' staple recessions and 3' staple overhangs. Repulsive helix ends were established by overhangs at both the 5' end the 3' staple ends. Neutral helix ends (neither attractive nor repulsive; only used for lid structure) were established by omitting end staples at the corresponding helices (see brown staples in the scheme).

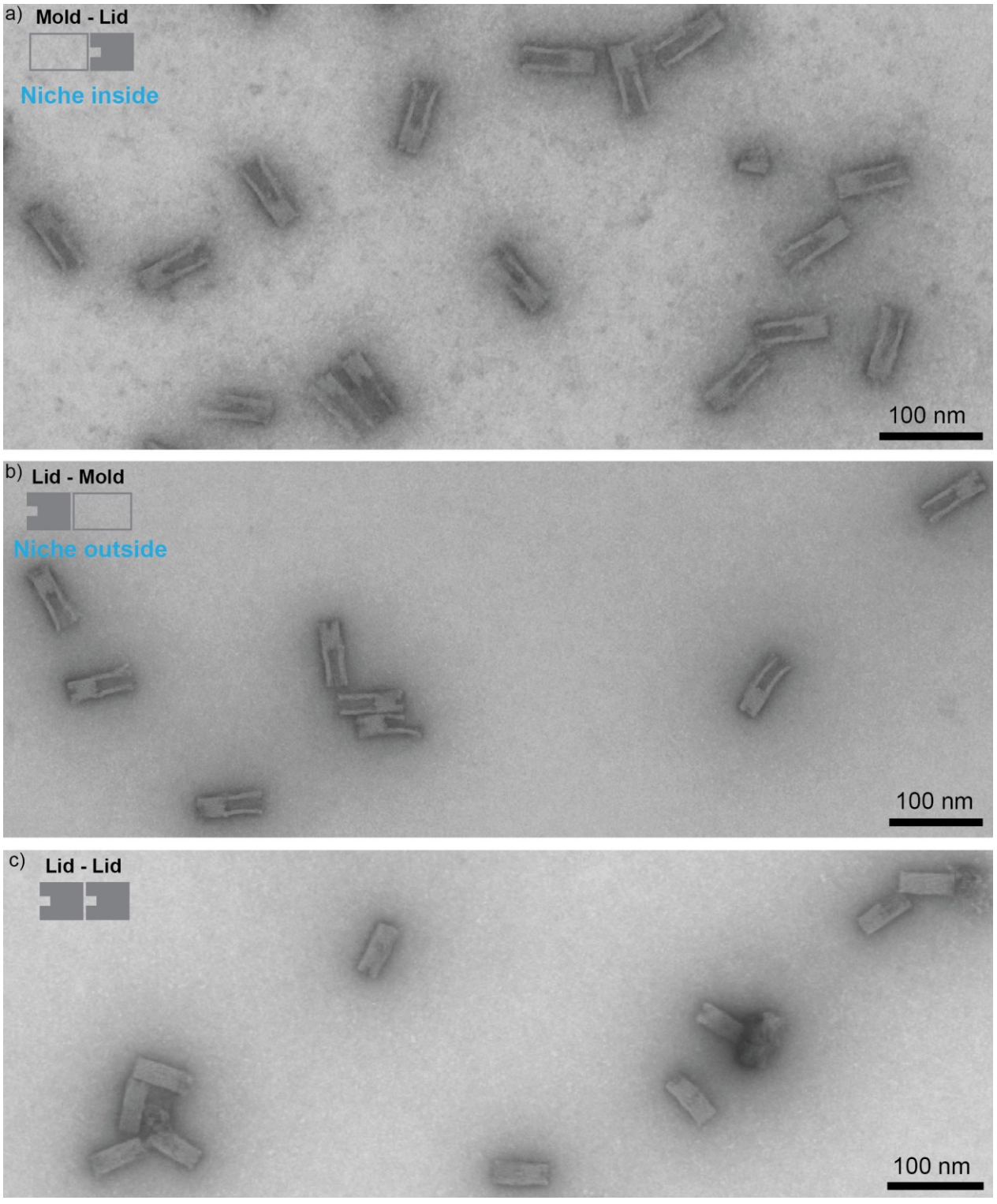

Figure S2. Overview tSEM images for dimer formation with lid elements.
(**a**) Lid-Mold dimer via the left lid end. (**b**) Lid-Mold dimer via the right lid end. (**c**) Lid-Lid dimer. Sketches show the expected orientation of the lid niche.

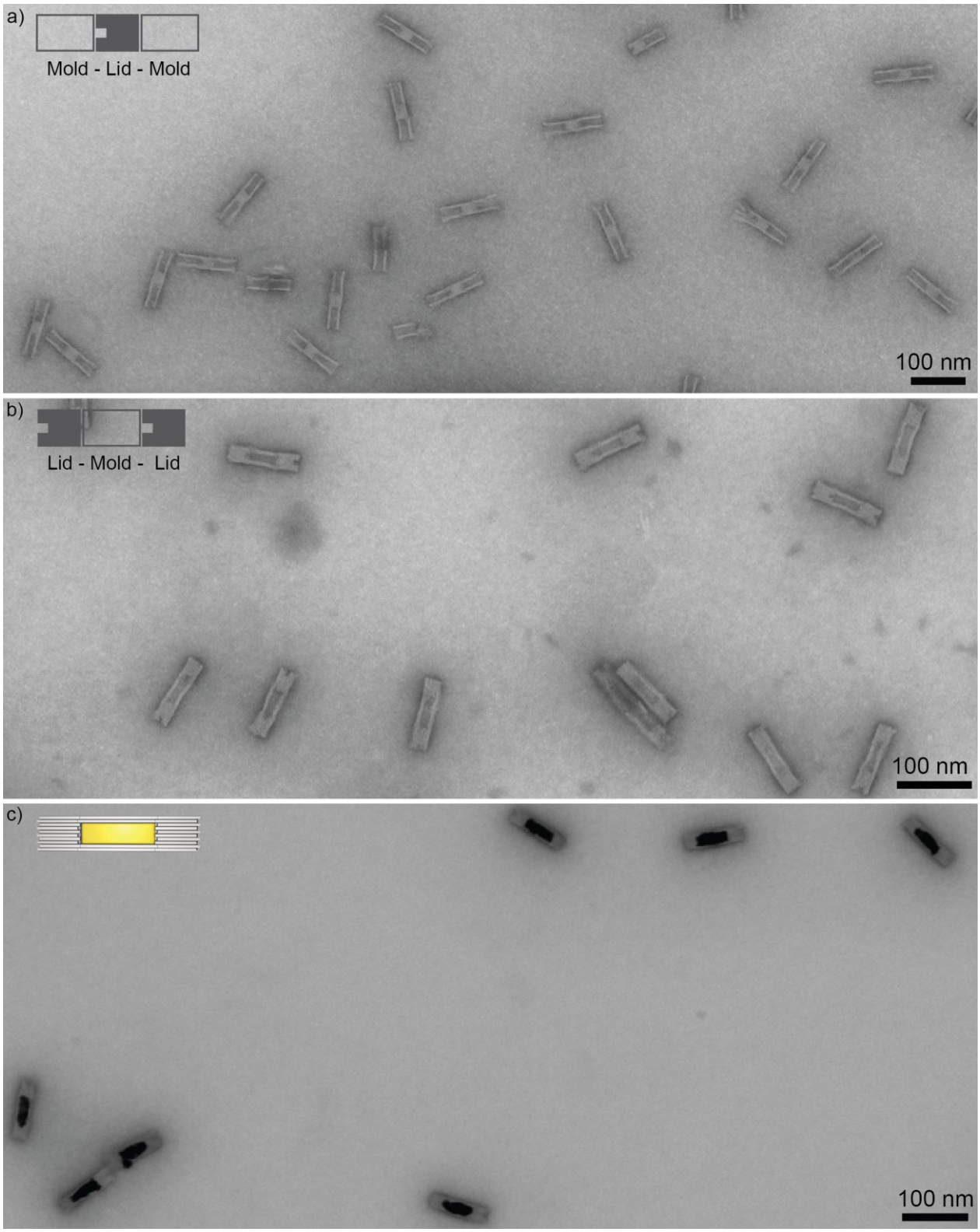

Figure S3. Overview tSEM images of Lid-Mold trimer structures.
(**a**) Mold-Lid-Mold trimers with the lid element in the center. (**b**) Lid-Mold-Lid timer structure with the mold element in the center such that a closed cavity/cage was. (**c**) Cage structures from (**b**) after loading with one seed and metal deposition. The cavity became filled with gold.

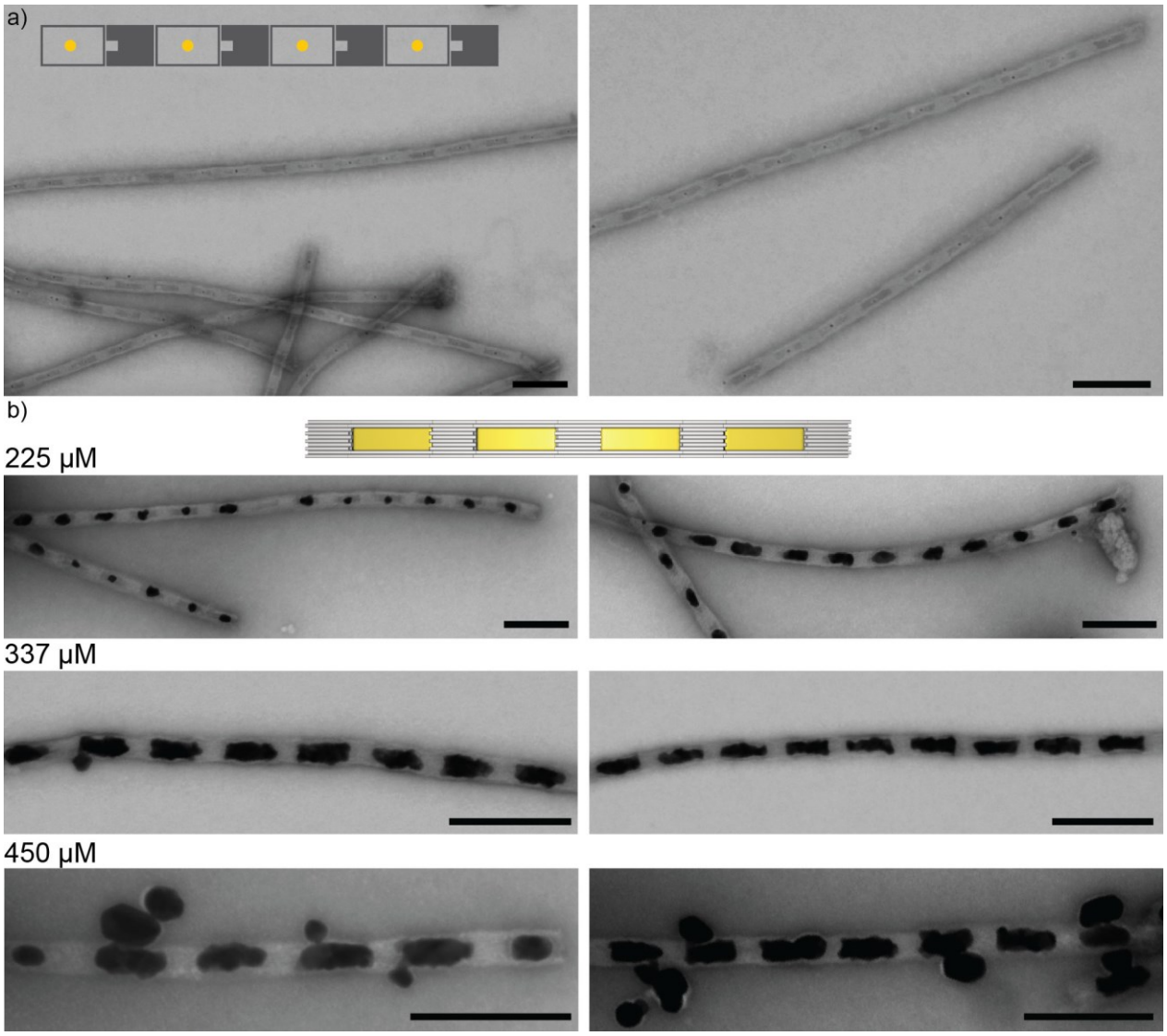

Figure S4. Alternating chain structures of lid and mold elements.
(**a**) tSEM images of alternating chains with lid and mold elements. Mold elements were preloaded with a single 5 nm AuNP. (**b**) Lid-Mold chains after metal deposition for different concentrations of gold precursor used in the deposition process. Scale bars: 100 nm.

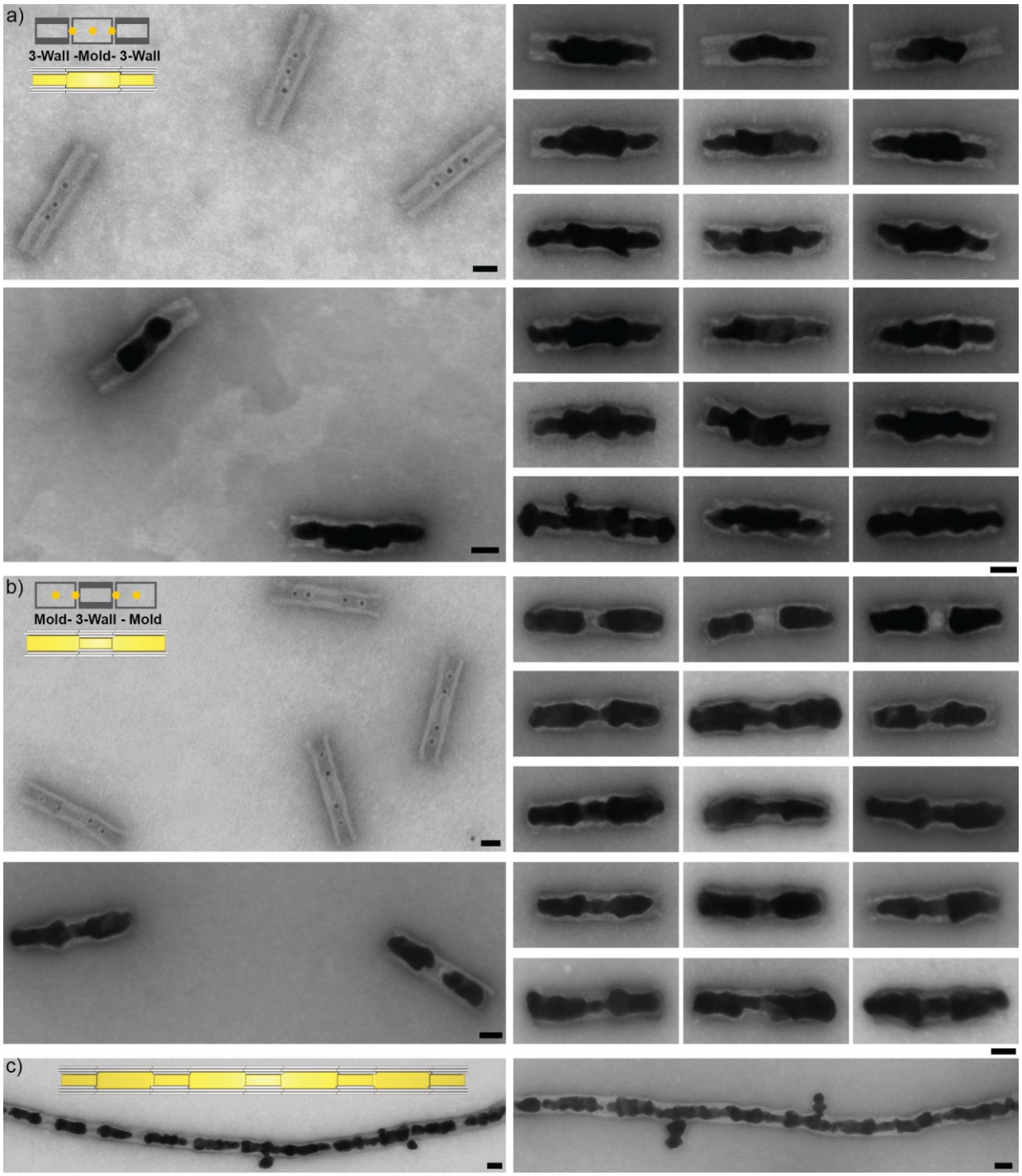

Figure S5. 3-wall-mold trimer structures.
(**a**) 3-wall-Mold-3-wall trimer structure preloaded with 3 AuNP seeds with the mold element in the center before (left upper corner) and after (left lower corner and right side) metal deposition. Resulting gold particles typically exhibited a 'rolling-pin' shape. (**b**) Mold-3-wall-Mold trimer structure preloaded with 4 AuNP seeds with the 3-wall in the center before (left upper corner) and after (left lower corner and right side) metal deposition. Resulting gold particles typically exhibited a 'dump-bell' shape. (**c**) tSEM images of alternating chains of mold and 3-wall elements after seeded gold growth exhibiting periodic constrictions of the diameter of the gold structure. Occasional defects result are due to lacking gold growth into the 3-wall element or due to lateral gold outgrowth at the interface between 3-wall and mold elements. Scale bars: 20 nm.

a)

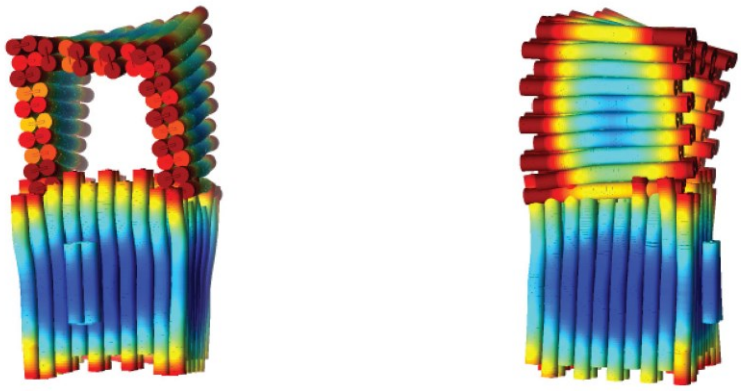

b)

Name	Start	End	Sequence
Zipper_1	2[103]	5[106]	AGTACAGTTTACTGTAGCGGTCACGCCCGATTTAGAGCTTGACG
Zipper_2	64[101]	2[104]	TACACTAGAATAACATAAAAACAGCAGCCTTACAACTGTACT
Zipper_3	4[106]	7[103]	GGGAAAGCCGGCGAACGTGCACCCAAATCAAGTACATGTATCAC
Zipper_4	7[104]	69[61]	GTGATACATTACCGCATCTGCGGAATCGATTAAGAGTAAATCAAGCAAAC
Zipper_5	10[103]	13[106]	ATAGCATGATACATAGCGAGAGGCTATGCAGATACATAACGCCA
Zipper_6	66[43]	10[104]	TACCTTTAAACAGTTCAGAATACTCATGCTAT
Zipper_7	15[104]	64[26]	GACCCTCGATACAATCCCCCTACACT
Zipper_8	12[106]	15[103]	AAAGGAATTACGAGGCATAACGGAACAACATTTACTCGAGGGTC
Zipper_9	38[106]	37[103]	TAAAGGAATTGCGAATAATATTGTATCGGTTTTACAACACGTCC
Zipper_10	37[104]	114[26]	GGACGTGTTTACAAAAAATCTACACT
Zipper_11	40[103]	39[106]	CTCAGCCCGTACGACGTTAGTAAATGAGAATAGAAAGGAACAAC
Zipper_12	112[47]	40[104]	ACGCAGAAAAAGCCGCACAGGCGGTACCGGGCTGAG
Zipper_13	46[106]	45[103]	GGCAAATCAACAGTTGAAAATTAGAGCCGTCATACTACGATAGG
Zipper_14	45[104]	111[65]	CCTATCGTATACGGAATTATCATGCGGTGTTGGCATATTCACGGGCTCTATACT
Zipper_15	48[103]	47[106]	CAGTGGCAGTACTGAGAGCCAGCAGAATCAATATCTGGTCAGTT
Zipper_16	114[101]	48[104]	TACACTACAAAGAAACCACCAGATTATCATTACCTGCCACTG

Figure S6. Junction element connections.
(**a**) CanDo simulation[3] of the junction element in which its top and bottom part are connected by single staple connectors. (**b**) DNA sequence for connectors based on the zipper geometry. Start and end positions of the staples correspond to the designs shown in Figure S25. Colored sequences represent 3 nt spacers (in red) and the zipper region, over which the two oligomers hybridize to each other (in green).

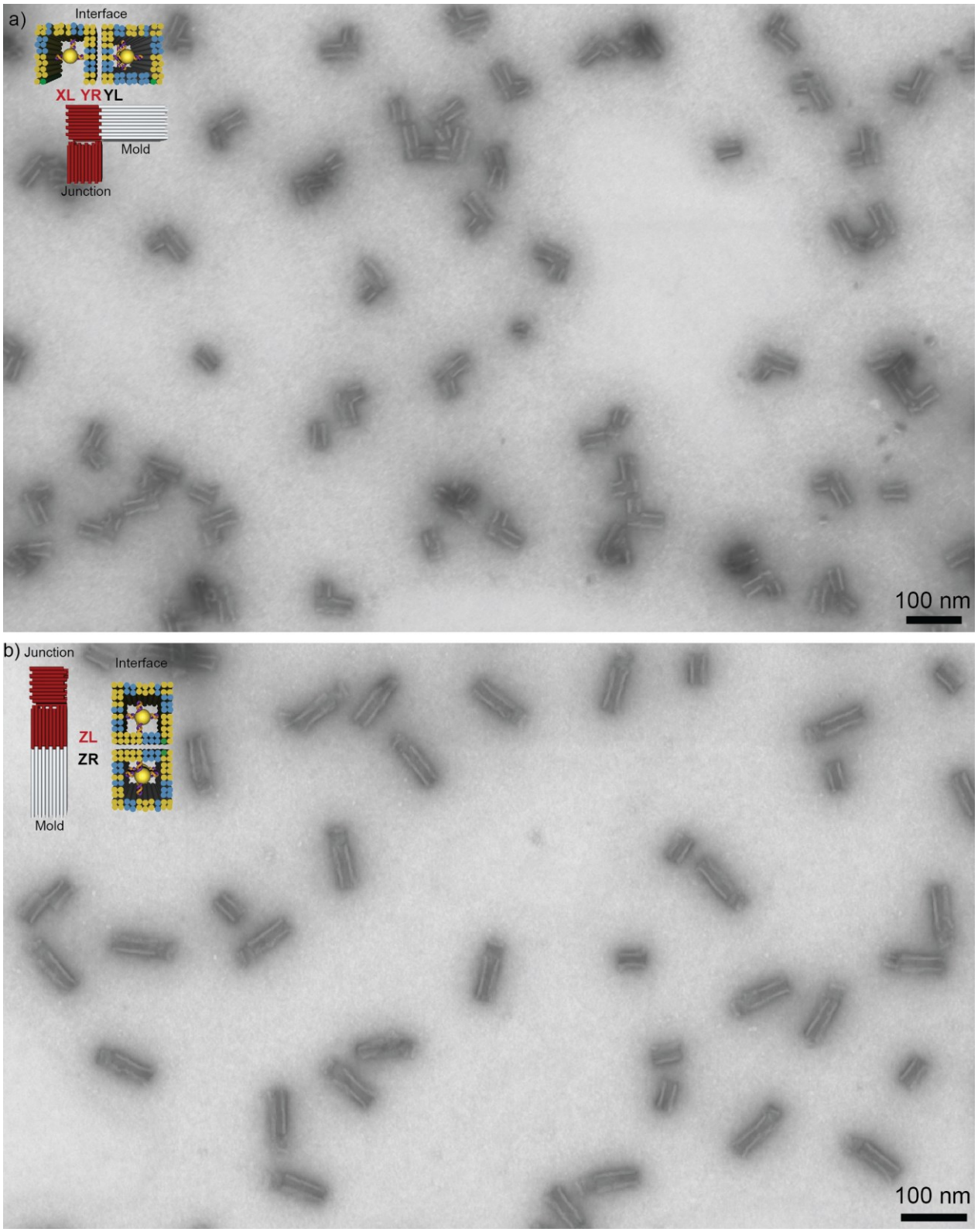

Figure S7. Overview tSEM images of Junction-Mold dimers.
(**a**) Mold docking to the right end of the top part of the junction via the Y interface. (**b**) Mold docking to the junction element´s bottom part via the interface Z. A high yield of the dimerization was achieved for both interfaces.

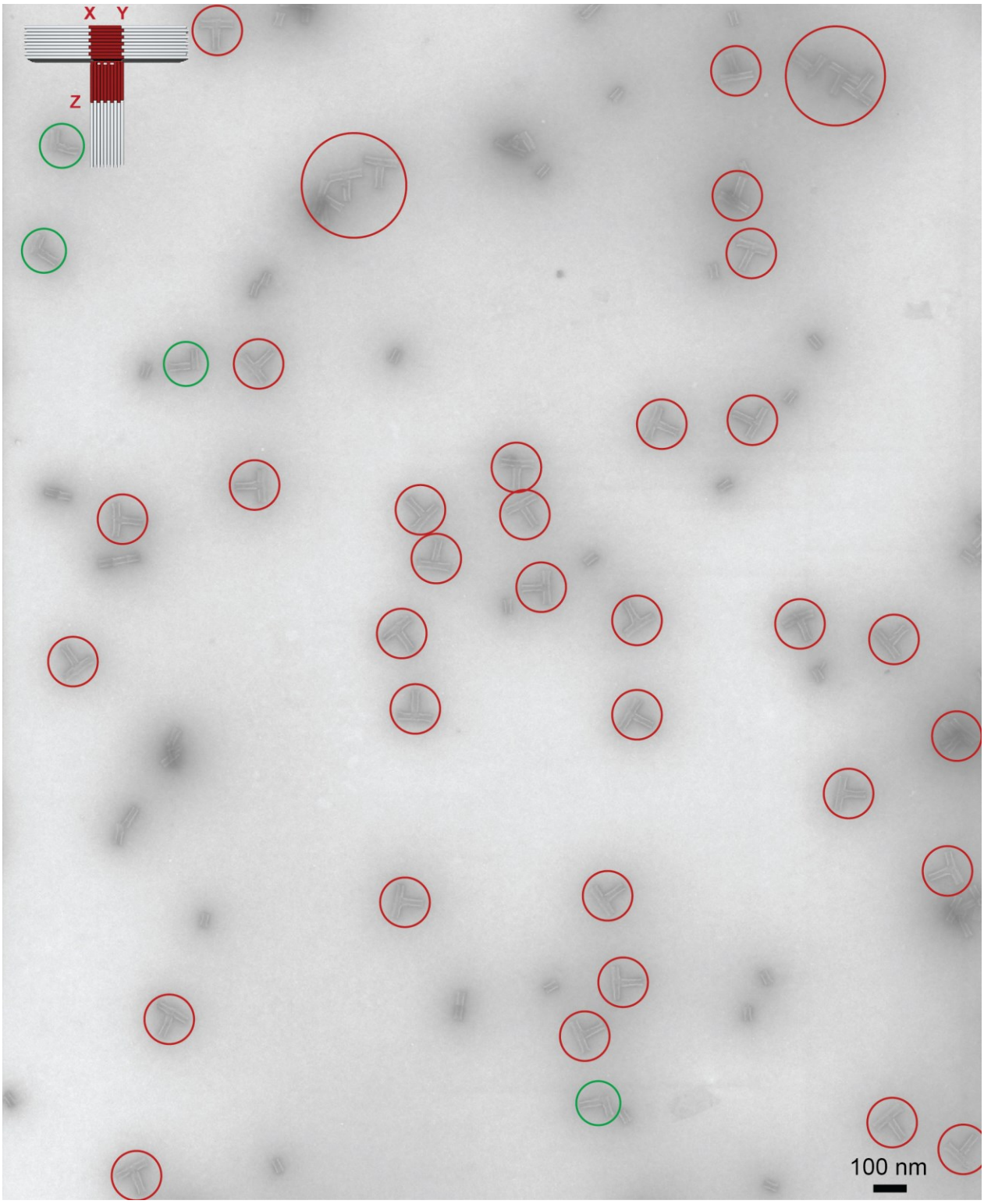

Figure S8. Overview tSEM image of T-shaped mold superstructures.
Three mold elements docked to a single junction element via the three available docking sites using the interfaces X, Y, Z (see sketch in upper left corner). Red circles mark correctly formed T-shape structures; green circles mark incomplete structures where one mold element is missing. The correct assembly yield of T-shaped mold superstructure is 72 ± 11%.

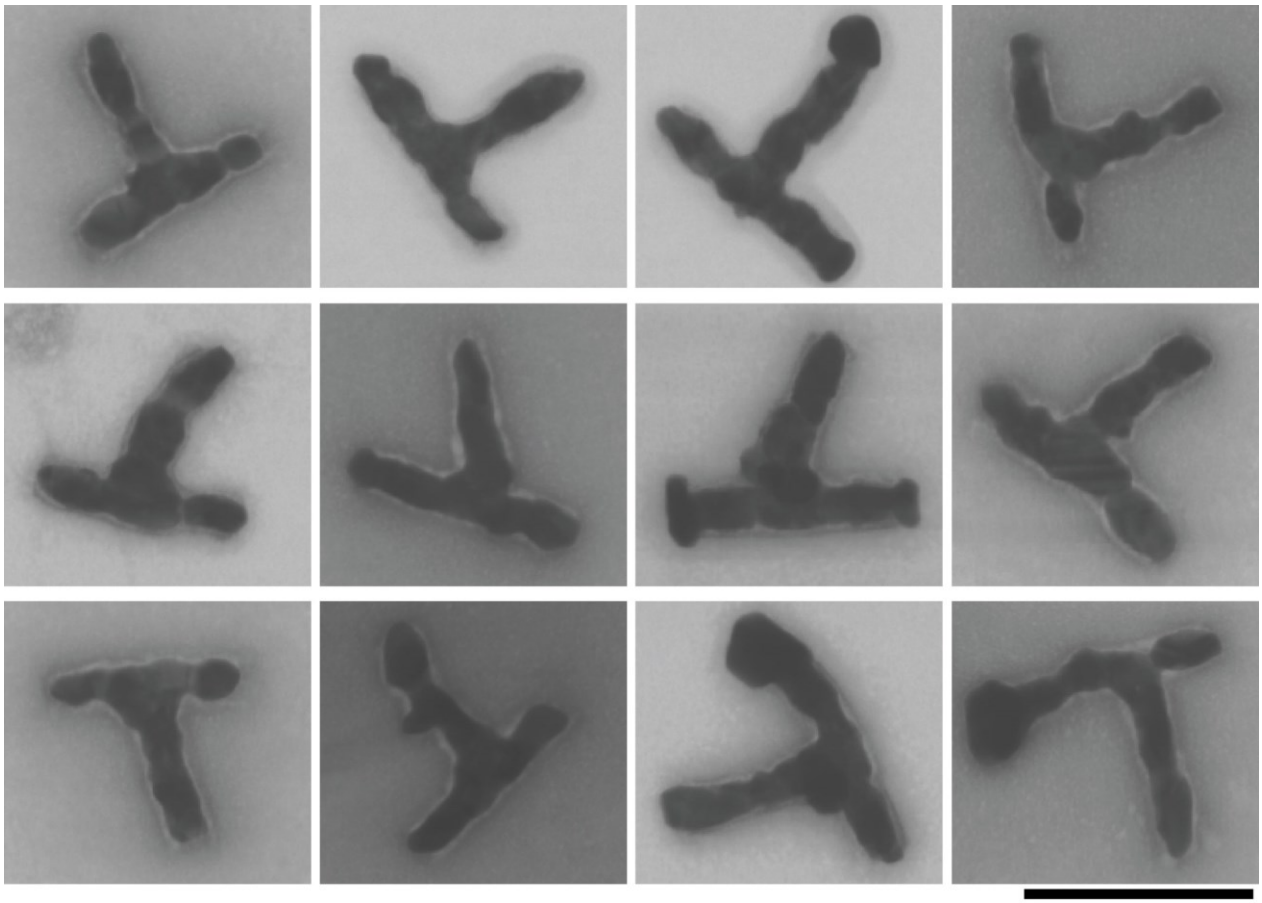

Figure S9. tSEM images of T-shaped structures after metallization.
T-shaped mold superstructures where the linear mold was preloaded with one 5 nm AuNP seed after metallization. Typically the shape programmed by the mold superstructure is reproduced. Deviations from the design include tilts of the T-stem as well as outgrowth of gold at mold ends. The correct assembly yield of square look structure is 61 ± 11%. Scale bar: 100 nm.

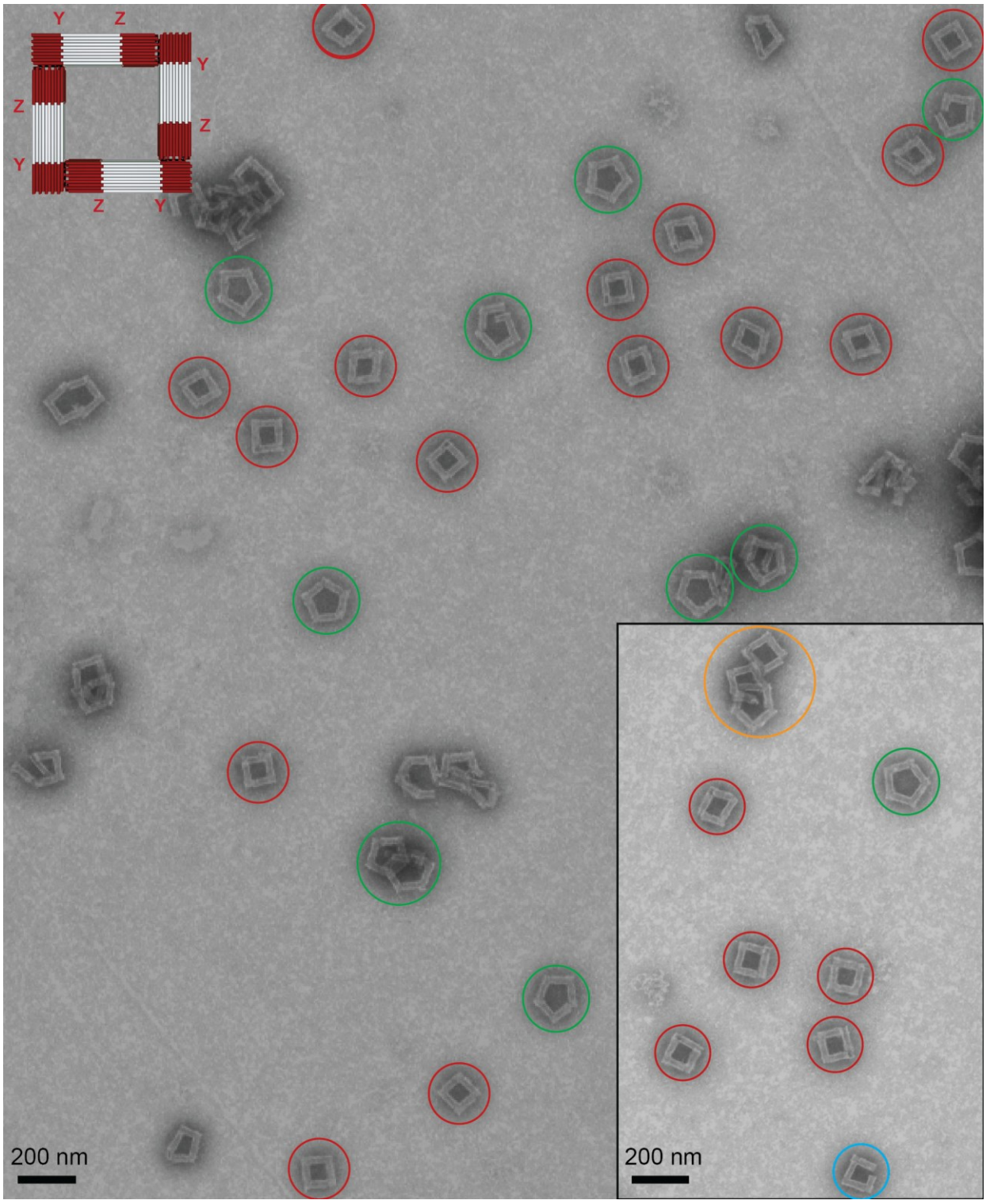

Figure S10. Overview tSEM image of square loop structures.
Square loop structures originate by self-termination from an alternating chain of junction and mold elements using the Y and Z interfaces. The resulting structures consist of 8 monomers (see sketch in upper left corner). The inset shows a sample spot with typical geometries found in the sample. Red circles mark correctly formed square loops; green circles mark pentagon loops; blue circles mark square loop structures that miss one element; orange circles mark aggregates of several structures. The correct assembly yield of square loop structure is 65 ± 15%

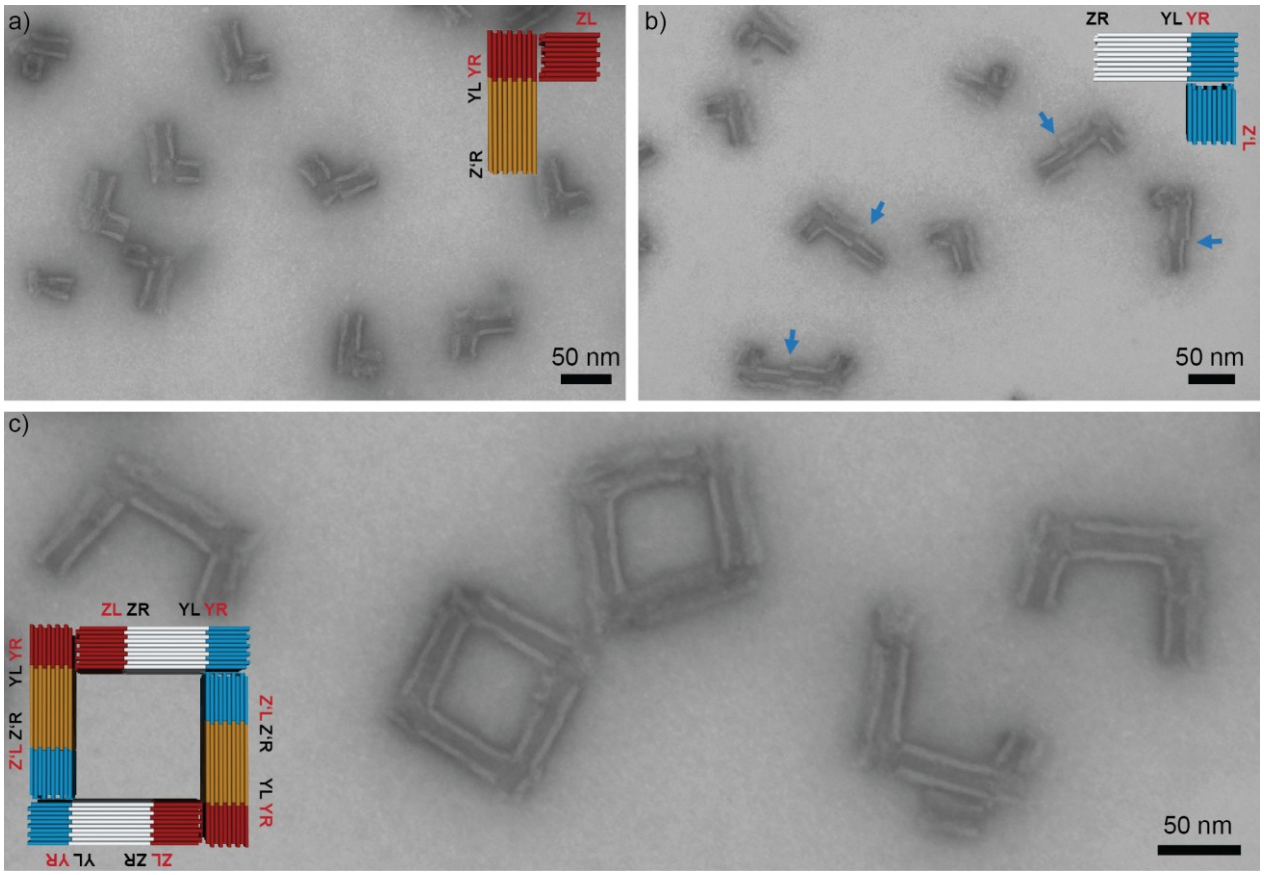

Figure S11. tSEM images of the assembly of square loop structures incorporating two variants of the Z interface.

Incorporating - in addition to interface Z - a weaker interface Z' on two opposing sides of the square should favor an initial formation of half squares (via Z) and in a second step the formation full squares rather than pentagon structures. (**a**) tSEM image of L-shaped Mold-Junction dimers with a right Z' interface and a left Z interface. (**b**) tSEM image of L-shaped Mold-Junction dimers with a left Z' interface and a right Z interface. Blue arrows indicated unspecific mold binding to the ZR interface. (**c**) tSEM image of square loop structures that were formed by mixing the two different L-shaped dimers at equal stoichiometry. An increased yield of square loops compared to the preparations with a single Z interface was not observed. The design of the Z' interface is shown in Figures S26.

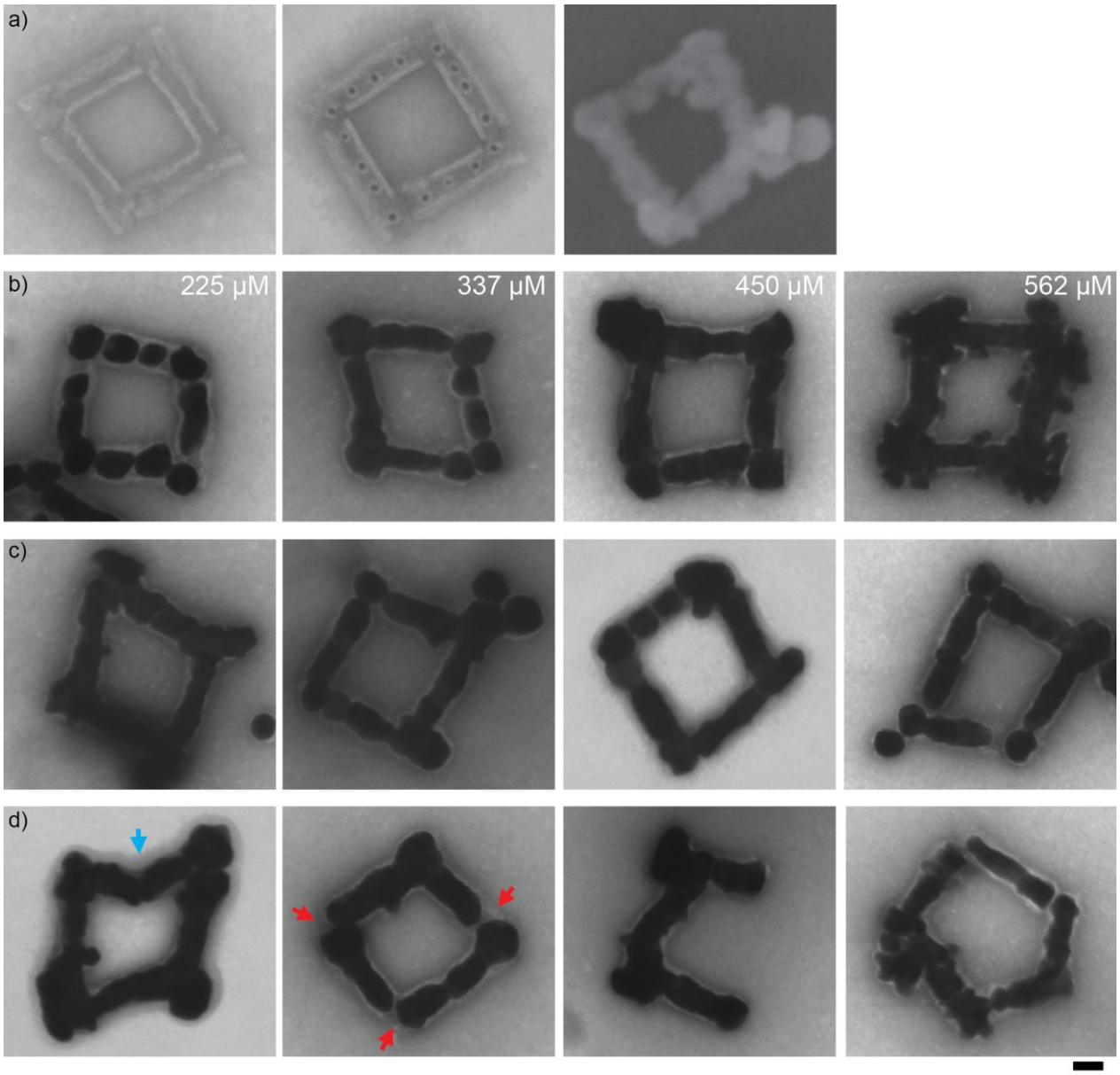

Figure S12. tSEM and SEM images of metallized square loop structures.
(**a**) tSEM images of square loop structures without seeds (left), preloaded with two AuNP seeds per mold monomer (center) and an SEM image of a square loop after gold growth and deposition on a SiO_2 substrate (right). In this case, the junction top was attached to the bottom part via 'single staple connectors'. (**b**) Metallized square loops for different gold precursor concentrations. (**c**) Metallized closed square loop structures. (**d**) Other geometries of the square loop, including bent edges, missing seeds, partial loop and pentagon structures. The correct assembly yield of metallized square loop structure is 29 ±10%. Scale bar: 20 nm.

Table S1. Yield of the different mold-based superstructures and metal nanostructures.

Superstructures	Mold superstructure	Metallized structure
Caged structure (lid-mold-lid trimer)	91 ± 4% (N=266)	87± 10% (N=203)
Rolling-pin-shape (3-wall-mold-3-wall trimer)	78 ± 16% (N=274)	78 ± 10% (N=241)
Dumbbell-shape (mold-3-wall-mold trimer)	81 ± 9% (N=221)	80 ± 8% (N=227)
T-shape (mold-junction tetramer)	72 ± 11% (N=225)	61 ± 11% (N=218)
Square loop (mold-junction octamer)	65 ± 15% (N=269)	29 ±10% (N=247)
Nanogap (mold-nanolid heptamer)	68 ±8% (N=252)	68 ±6% (N=231)

Note S2. Network fabrication with connector element.

The square loop geometry was employed to realize even larger network structures. For this, we designed a dimeric connector element with a right X' interface (modified X interface) on each end, such that it could bridge between the corners of two square loops (left X' ends). As connector monomer we employed a linear mold element with one left X' interface. Its left end was designed to allow self-dimerization (Figure S13a). The self-dimer could form with a second connector being rotated by 180° in the image plane of the network (Figure S13b). When folding the connector monomer without end staples at the dimerization interface, only monomers were obtained (see Figure S13c). In the presence of the end staples at the dimerization interface, the formation of self-dimers at high yield was observed (see Figure S13d). When mixing the square loop with this monomer, the four available docking sites on the square became occupied (Figure S13e).

A single connector dimer can connect two square loops (see scheme in Figure S13f), which appear to be turned by 180° with respect to each other. When mixing assembled square loops and connector dimers, such structures consisting of 18 origami elements could be found by tSEM imaging (see Figure S13g). Using additional connector dimers larger periodic network structures should form by periodic interconnections of square loops in a 2D plane. tSEM imaging revealed the formation of larger structures according to this design (Figure S14). However, in these structures assembly defects accumulated, such that very large periodic structures were not observed. The presence of uncovered mold ends supported furthermore the aggregation of these networks (Figure S15a). Preloading the mold monomers before network assembly allowed the metallization of the mold networks (Figure S15b), which shows that metal network structures can generally be obtained by specifically "programming" the interfaces of linear mold and junction elements. Aggregation was however limiting the yield of obtained metal network structures.

Generally, lower efficiencies were obtained for the structures comprising closed square loops (bearing four junction elements, e.g. Figure S10). Main problem in here is the flexible attachment between the top and the bottom part of the junction element providing often incomplete or non-square polygonal loops. These limitations should be overcome by a redesign of the junction element to make it more rigid (Figure S11a) and the introduction of specific interfaces for the loop, allowing a defined step-wise assembly of multiple junction-mold dimers. An efficient loop closure will most likely also prevent aggregation of the loop networks, since this was only observed in this type of samples, but not for the T-shape structures. In turn, this should allow the high-yield formation of even larger programmable structures.

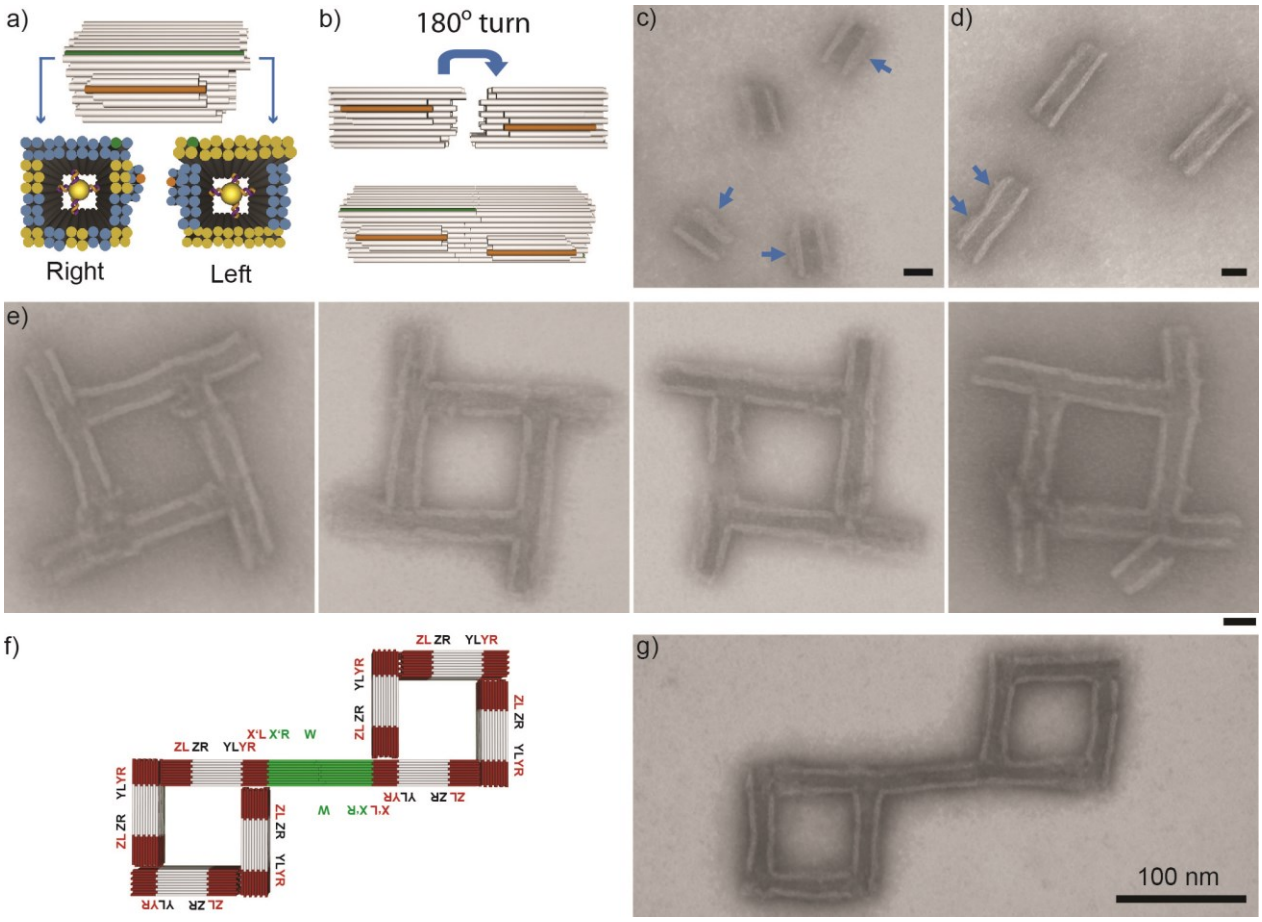

Figure S13. Connector element for square loop structures.

(**a**) Scheme of connector element monomer (top) and the interface designs for the left (supporting self-dimerization) and the right end (bottom). Helix 0 is shown in green; a helix shown in orange is used as an orientation marker. **(b)** Scheme of self-dimerization of the connector monomer via its left end with a second element that is turned by 180° in the image plane. (**c**) tSEM image of connector monomers in absence of an attractive dimerization interface. The helices extruding from one of the sides are marked with blue arrows. (**d**) tSEM image of connector dimers with in presence of an attractive dimerization interface. (**e**) tSEM images of the square loop structures with bound connector monomers on all corners of the square. (**f**) Scheme of two square loops interconnected by a connector dimer. (**g**) tSEM image of two interconnected square loops. Scale bars without labels correspond to 20 nm.

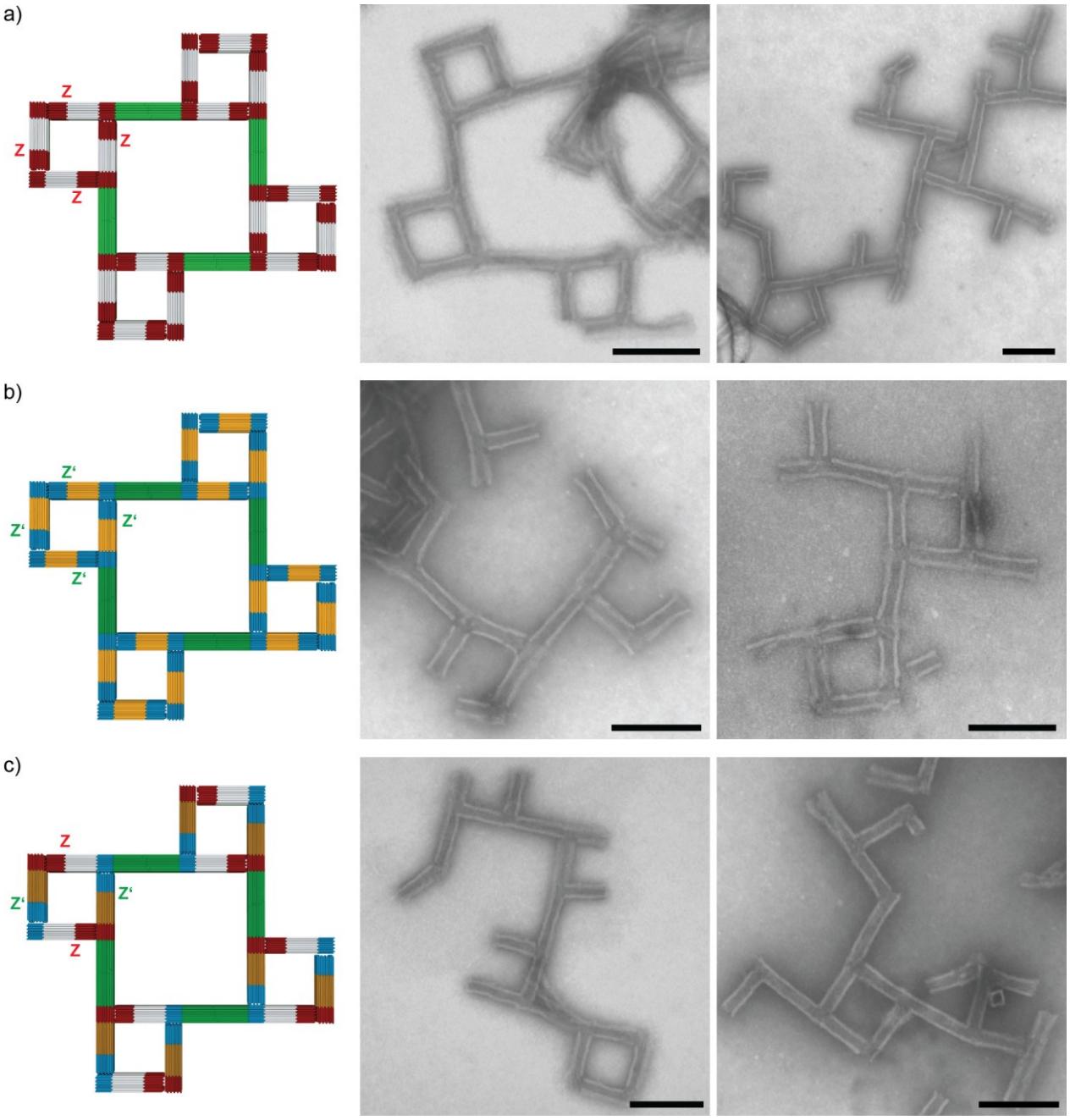

Figure S14. tSEM images of formed network structures.
Networks were formed by mixing preassembled square loop structures with connector dimers at equal stoichiometry. The left side of each subfigure shows the design scheme. Networks were formed using square loop structures that were formed using (**a**) only interface Z (**b**) only interface Z’ and (**c**) an equal mixture of Z and Z’ interfaces. Scale bar: 100 nm.

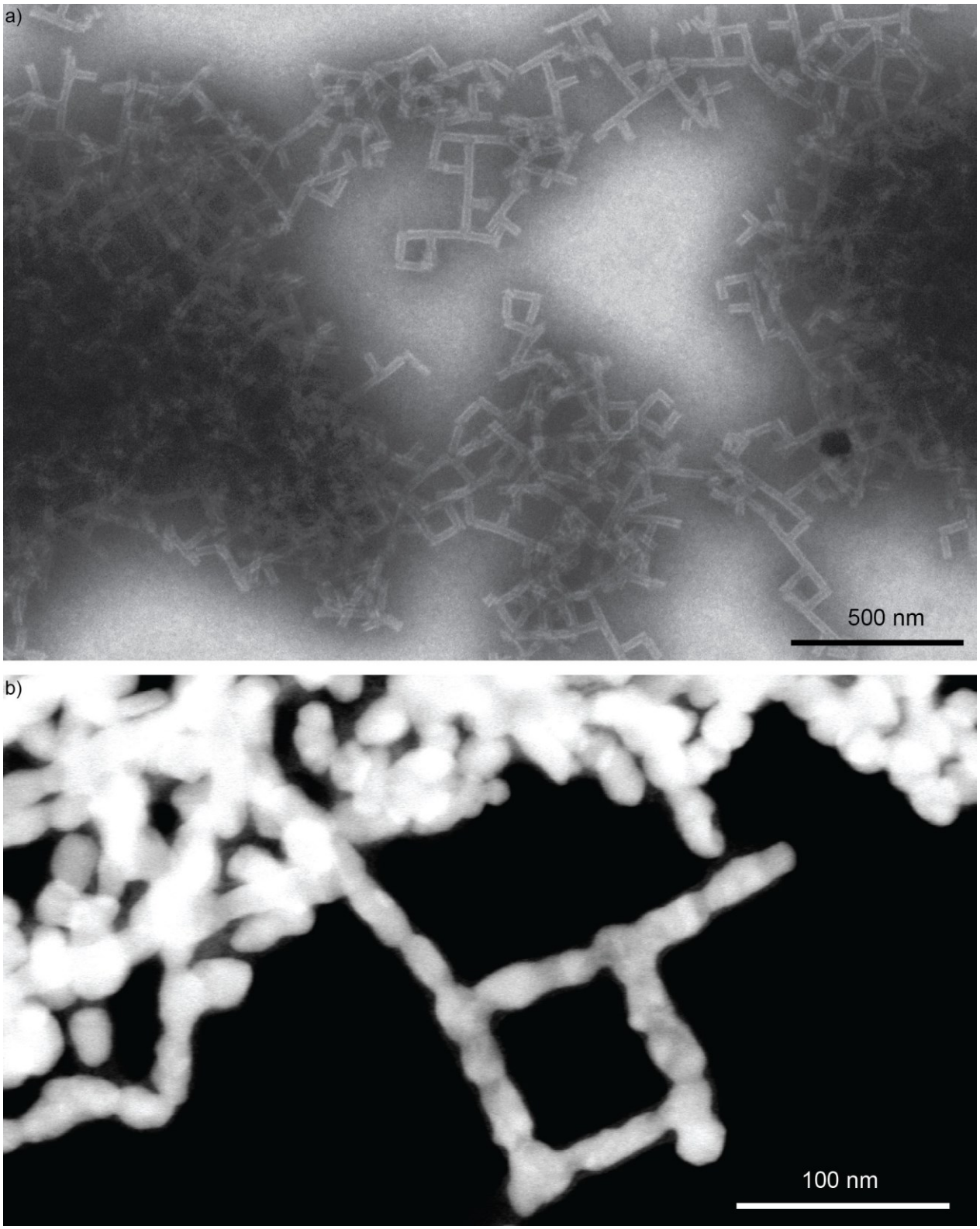

Figure S15. Network structures before and after metal deposition.
(**a**) Mold network structures had a considerable tendency for aggregation due to a considerable number of assembly affects that provided unpaired ends. (**b**) Network structure after the metal growth reproducing typical design elements of the network (dark field tSEM image). Aggregation between the metallized structures was too strong to reveal larger periodic structures.

Note S3. Optical characterization of the metallized L- and T-shaped metal structures.
For the electromagnetic simulations, perfectly matching-layer boundary conditions were set in all principal directions, as shown in Figure S16. Monitor boxes were used to obtain the optical responses of the system. The frequency points were matching the wavelength span of the source. For the dielectric properties of gold, the data from Johnson and Christy[4] was fitted using a 6th order polynomial function, with a root-mean-square (RMS) error of 0.25. All simulations reached an auto-shut-off of at least 10^{-5} before reaching 300 fs of the simulation time. For the best simulation stability, the mesh step size was set to 0.25 nm in all three principal directions.

To determine the optical properties of the synthesized structures, single-particle spectroscopy was performed. The scattering cross-section for both types of particles was revealed to be compliant with the simulated spectra (see Figure S17c and S17f). For T-shaped structures, the signature of the longitudinal mode at 784 nm is present, whereas for the L-shaped structure it is blue-shifted to the 650 nm, due to the smaller size along the x-axis. The transversal mode features higher energy and can be recognized at 608 nm. The apparent deviations of the experimentally measured spectra can be explained by the shape variations of the nanostructure, which was not considered in the simulations. The scattering spectrum and thus the resonance wavelength of the plasmonic modes are very sensitive to changes in dimension, shape and material[5]. In this case, however, for representative T- and L-shapes, only corner and edge rounding was considered in the simulations.

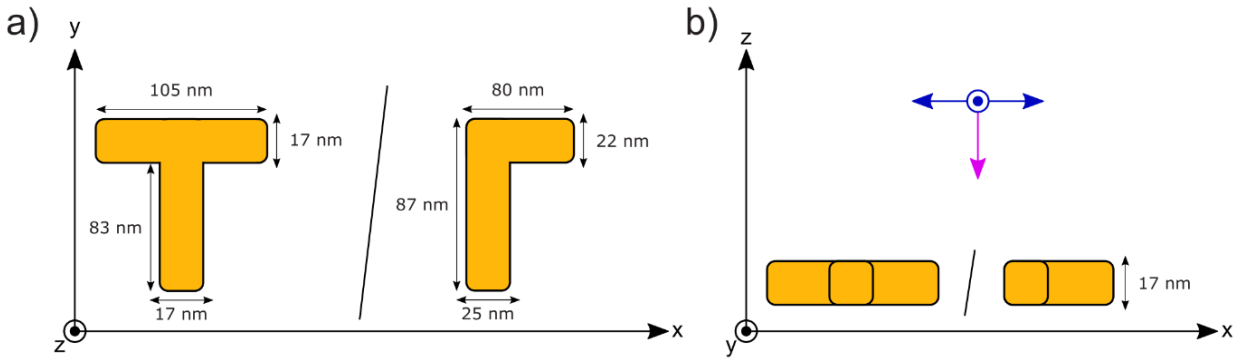

Figure S16. Electromagnetic simulation (FDTD) dimension scheme.

(**a**) In-plane view of the schematic representation of the T- and L-shaped structures. (**b**) Side view of the structures illuminated by the light source. The purple vector shows the propagation direction and the blue vector the polarization of the electric field of the plane wave source.

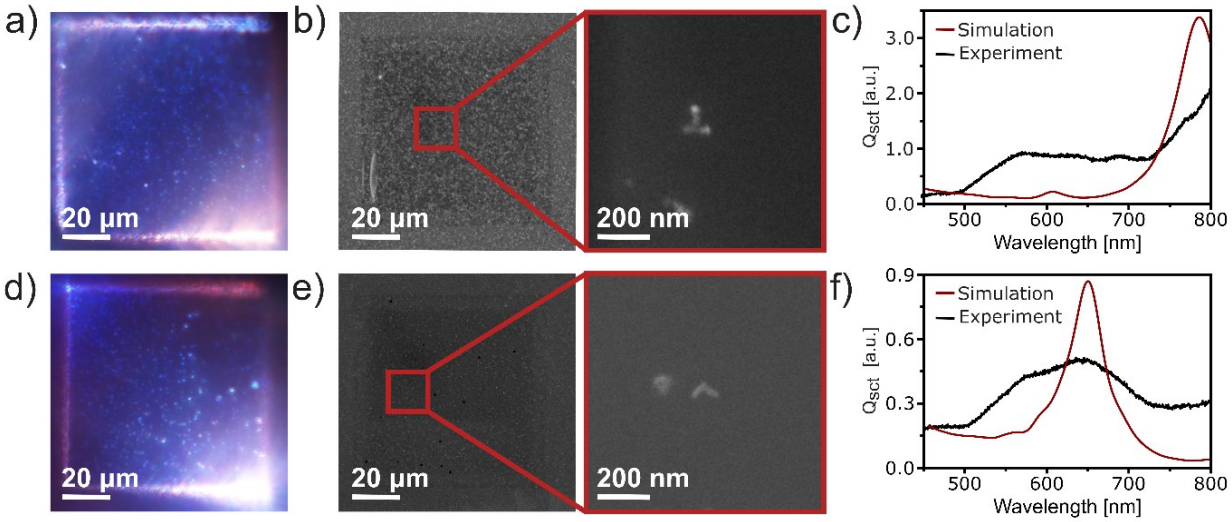

Figure S17. Dark-field microscopy and spectroscopy of the T- and L-shaped structure.

(**a**), (**d**) Dark-field images of the selected TEM grid, where T- and L-shaped structures were located. (**b**)**,** (**e**) SEM images of the corresponding particles. (**c**)**,** (**f**) Measured single-particle spectra of the scattering cross-section together with the corresponding simulations of the spectra.

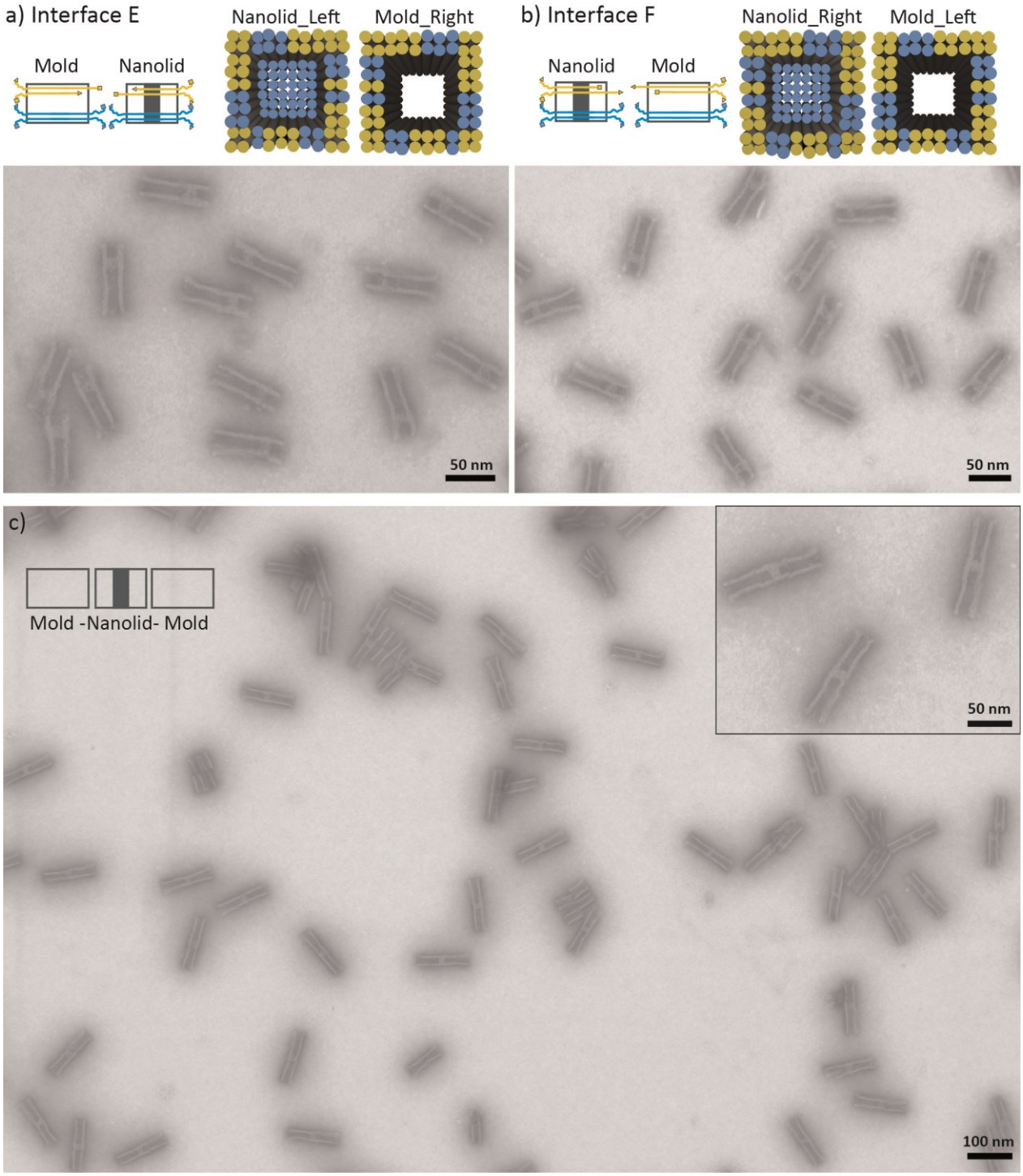

Figure S18. Fabrication of nanolid-mold dimer and trimer structures.

(a-b) Interfacing the nanolid element with a standard mold element at either end. Top: Design scheme of the nanolid-mold interfaces (interfaces E and F). Attractive and repulsive helix ends are shown in yellow and blue, respectively. Bottom: TEM images of the mold-nanolid dimers exhibiting assembly yields of 97±2% (N=211) for interface E and 98±2% (N=209) for interface F. **(c)** TEM overview image of the mold-nanolid-mold trimer structure. The assembly yield of the trimer structure reached 90±5% (N=256).

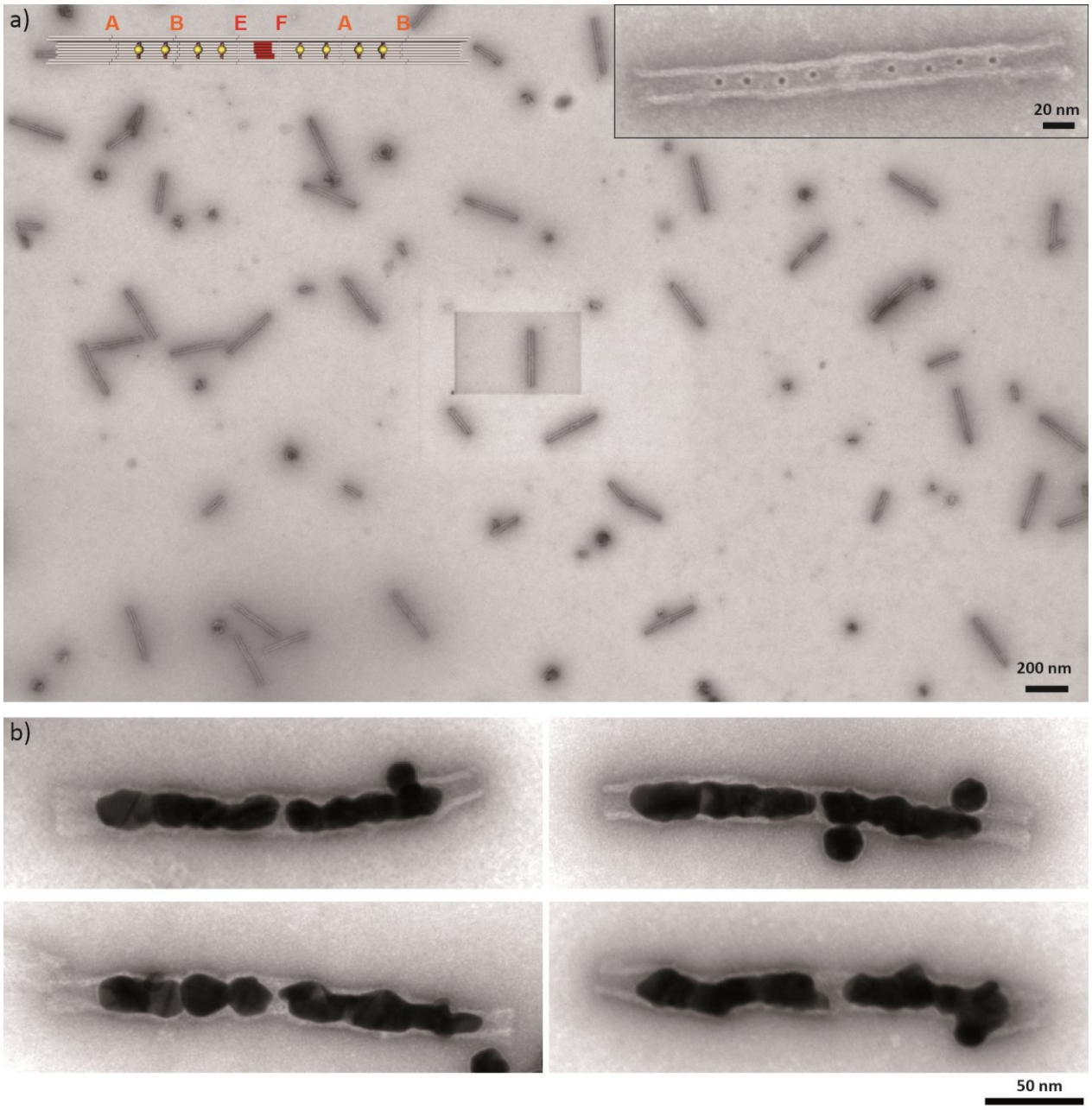

Figure S19. TEM images of the DNA nanolayer integrated into a mold heptamer before and after metallization.

(a) TEM overview image of the DNA nanolid structure with three AuNP-loaded mold elements at either end (see scheme at the top left) before the seeded gold growth (corresponding to Figure 5a, b in the main text). The correct assembly yield is 68 ±8%. **(b)** TEM images of the heptameric structure after metallization after which the DNA nanolayer became contacted by nanoelectrodes of ~100 nm length.

Note S4. Integration and electrical characterization of DNA nanolayers.

For creating electric contacts to the metallized DNA origami assemblies, large contact pads in combination with alignment markers for later positioning were fabricated on a SiO_2/Si substrate. The DNA nanolayer-nanoelectrode assemblies were then deposited from solution onto these substrates using the recipe as previously described.[1] The DNA assemblies were first characterized by scanning electron microscopy, and the positions of suitable structures was recorded for subsequent contacting. Gold contacts to connect the DNA nanolayer-nanoelectrode assemblies to the large contact pads were then defined using electron beam lithography (EBL) using a precise alignment procedure based on the pre-defined markers. In order to ensure good electrical contacts to the Au nanoelectrodes, which have been self-assembled inside the DNA molds, the surrounding DNA needed to be removed by oxygen plasma (PICO, Diener Electronic-Plasma Surface Technology). Since this step would also remove the DNA nanolayer situated in between the Au nanoelectrodes, the DNA nanolayer was first protected using a locally defined patch of HSQ (hydrogen silsesquioxane) resist (Figure S20a). HSQ becomes electrically insulating after exposure and development. For protection, the substrate was spin coated with 2% HSQ and post baked at 120°C for 4 min. The resist was exposed during electron beam lithography at an area dose of 1200 μC/cm^2 in the vicinity of the DNA nanolayer. HSQ was developed for 15 sec in an aqueous solution of 25% TMAH (Tetramethylammonium hydroxide), followed by 30 sec in MF319 (Microposit) and subsequently rinsed in DI water as well as isopropanol and finally dried in a N_2 stream.

For the fabrication of the metallic contacts, the substrate was spin coated with ZEP520A resist (Zeon, Japan) and baked at 150°C for 10 min. The resist was exposed at an area dose of 35 μC/cm^2 to define the contact electrodes for the Au nanoelectrodes. Subsequently, a 5 nm adhesive Ti layer followed by a 70 nm Au layer were deposited at 0.2 Å/s and 2 Å/s, respectively, using electron beam evaporation. Lift-off of the metal layer was done by immersion in dimethyl acetamide**.** Subsequently, the samples were rinsed with isopropanol and dried in an N_2 stream to provide the final contacted DNA nanolayer assemblies (Figure S20b-c).

The resulting structures were electrically characterized at various temperatures from room temperature down to 4 k in a cryogenic probestation (LakeShore) using an Agilent parameter analyzer (4156C). For recording I-V curves, the voltage applied between the two contacts was swept from -4V to +4V while measuring the corresponding current. Various DNA nanolayer structures could be tested within one cooling cycle, thus minimizing the time necessary for analyzing multiple configurations.

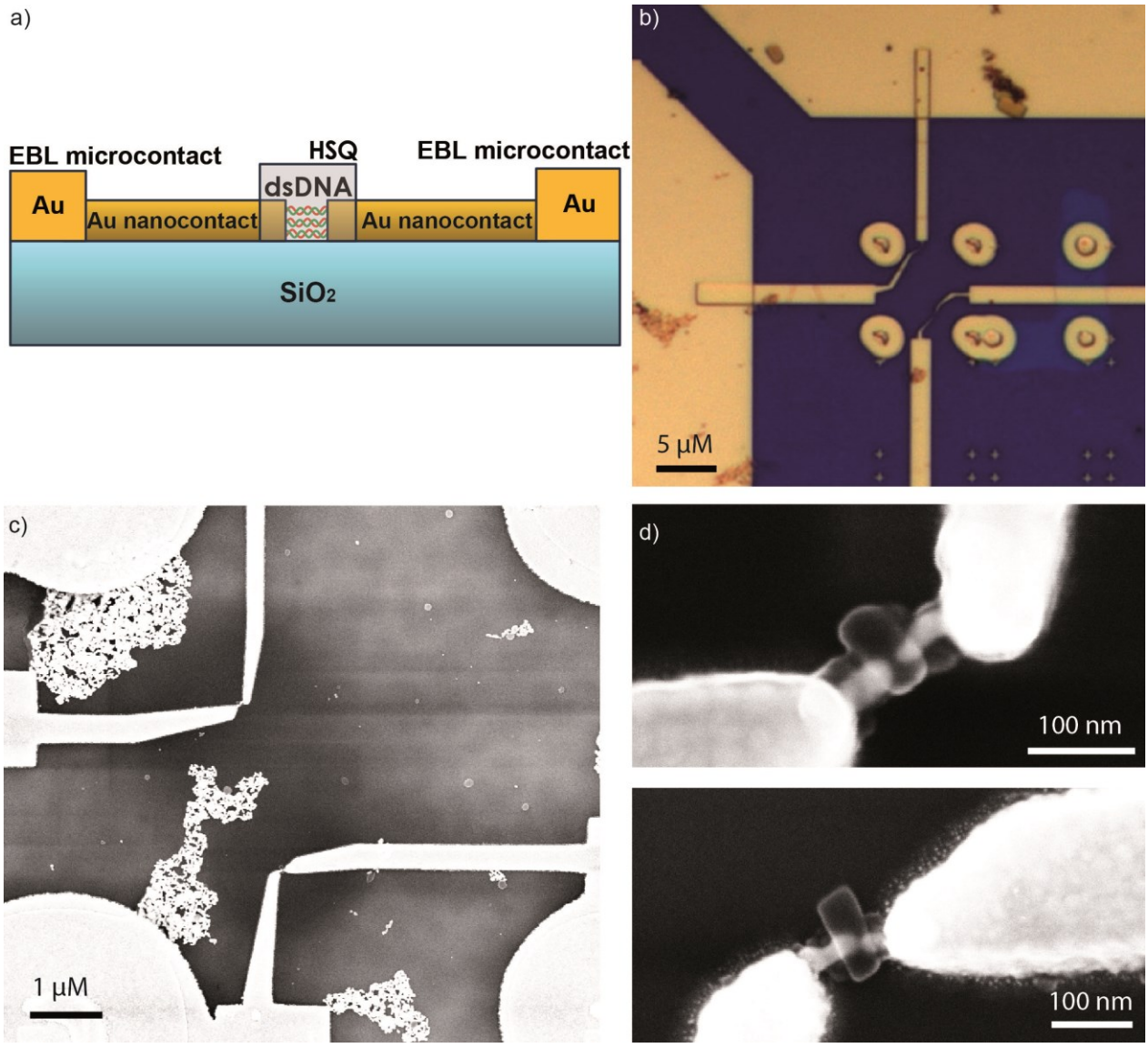

Figure S20. The gold contact fabrication scheme.

(a) Sketch of the contacting scheme of the DNA nanolayer-nanoelectrodes assembly using electron beam lithography. The DNA nanolayer was protected by HSQ resist to avoid damaging during the EBL procedure. **(b)** Optical microscope image of the contacted DNA nanolayer-nanoelectrode assembly showing the large contact pads and the metallic connections between these pads and the nanoelectrodes. **(c)** SEM overview image of two contacted DNA nanolayer devices. **(d)** Enlarged view onto the two contacted DNA nanolayers with an HSQ patch on top of the DNA.

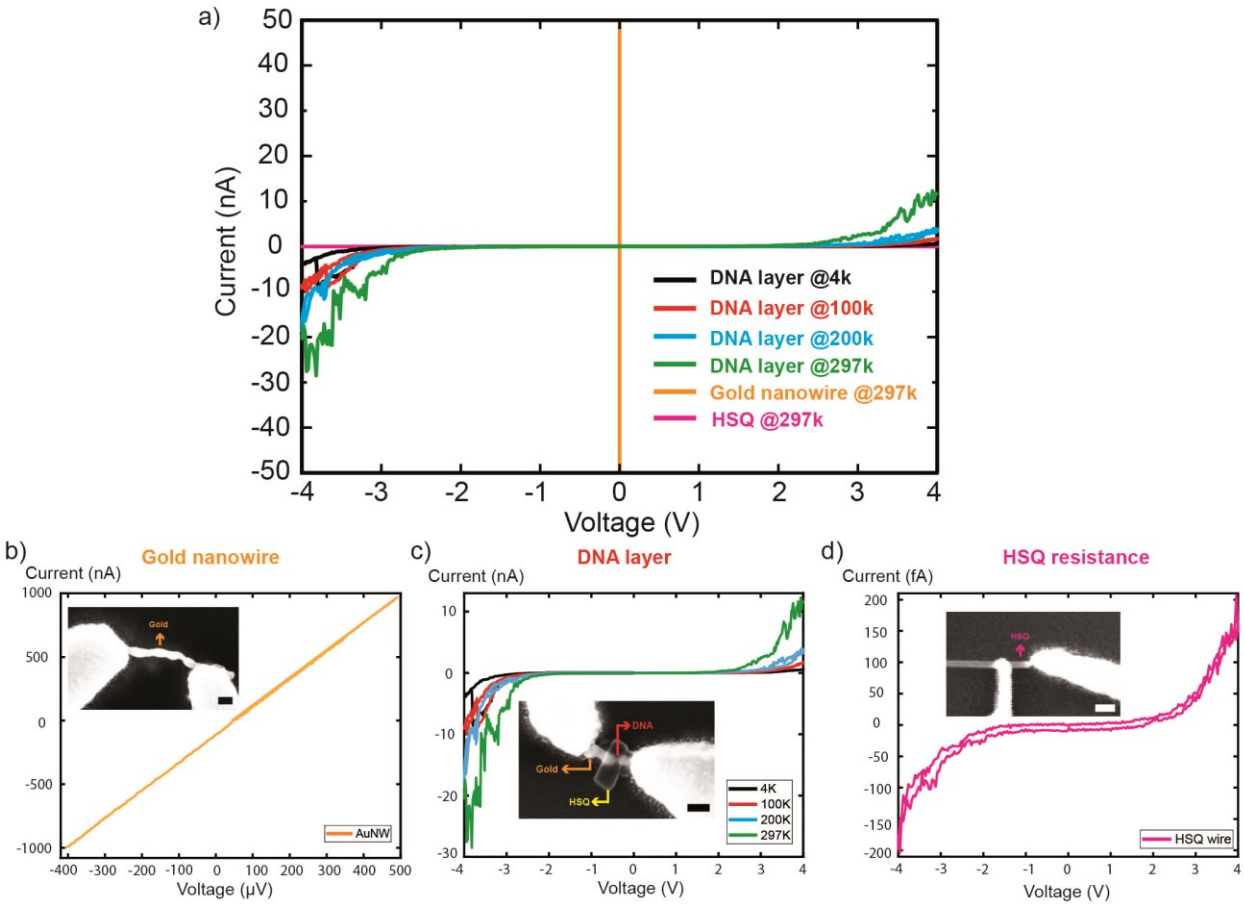

Figure S21. Electric characterization of gold nanowire, gold nanogap and HSQ.

(a) Comparison of the current-voltage characteristics of a continuous gold nanowire (in orange), the bare HSQ resist (in magenta) and a DNA nanolayer (different sample than shown in main text). The DNA nanolayer was characterized at different temperatures as indicated, while the other two samples were characterized at room temperature. **(b-d)** Enlarged views on the current-voltage characteristics of gold nanowire, DNA nanolayer and HSQ resist. Insets show SEM images of the samples after integration with EBL. Scale bars: 50 nm.

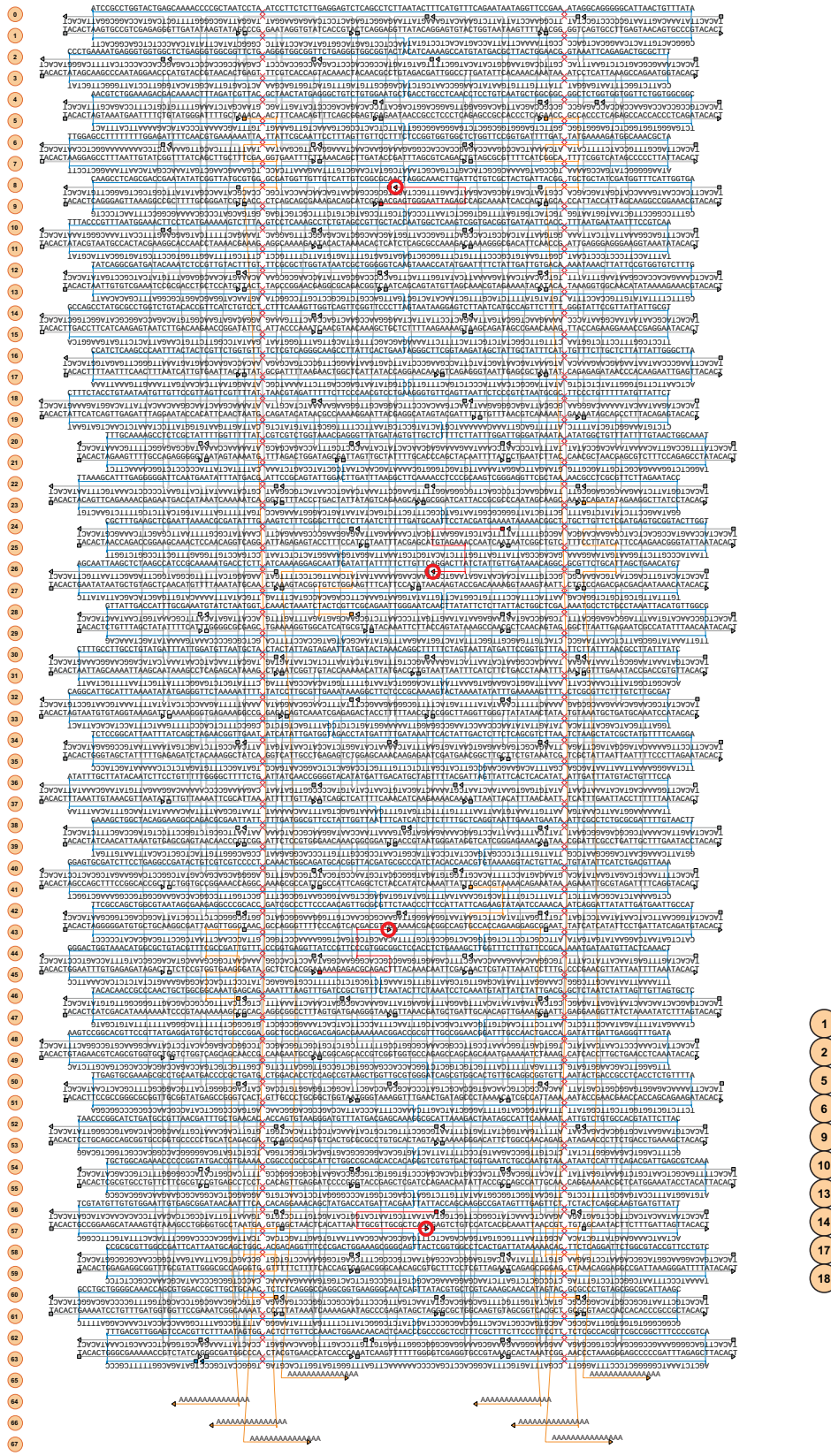

Figure S22. Design template of the standard *mold element.*
Sequence and folding of the 8064 nt scaffold (blue) and the staples used to form the structure. The depicted mold element carried only repulsive ends. The repulsive ends carry 5'-TACACT ssDNA extensions at the 5' and 3'-ends. Staples in yellow represent the capture strands that carry 15 nt 3'-polyadenine overhangs for attaching two DNA-coated AuNP seeds. Red circles indicate the position of the 15 nt 3'-polyadenine overhangs used to attach a single AuNP seed. Squares and triangles at the staple ends symbolize the 5'- and the 3'-end, respectively. The core design template was created using CaDNAno[6]. Red crosses are imaginary gaps that were introduced for better graphical representation. This was done in order to fit the 8 bp lattice size (corresponding to about 270° turns) into the 63 bp unit cell (six helical turns of dsDNA) that underly the square-lattice arrangement of DNA helices.

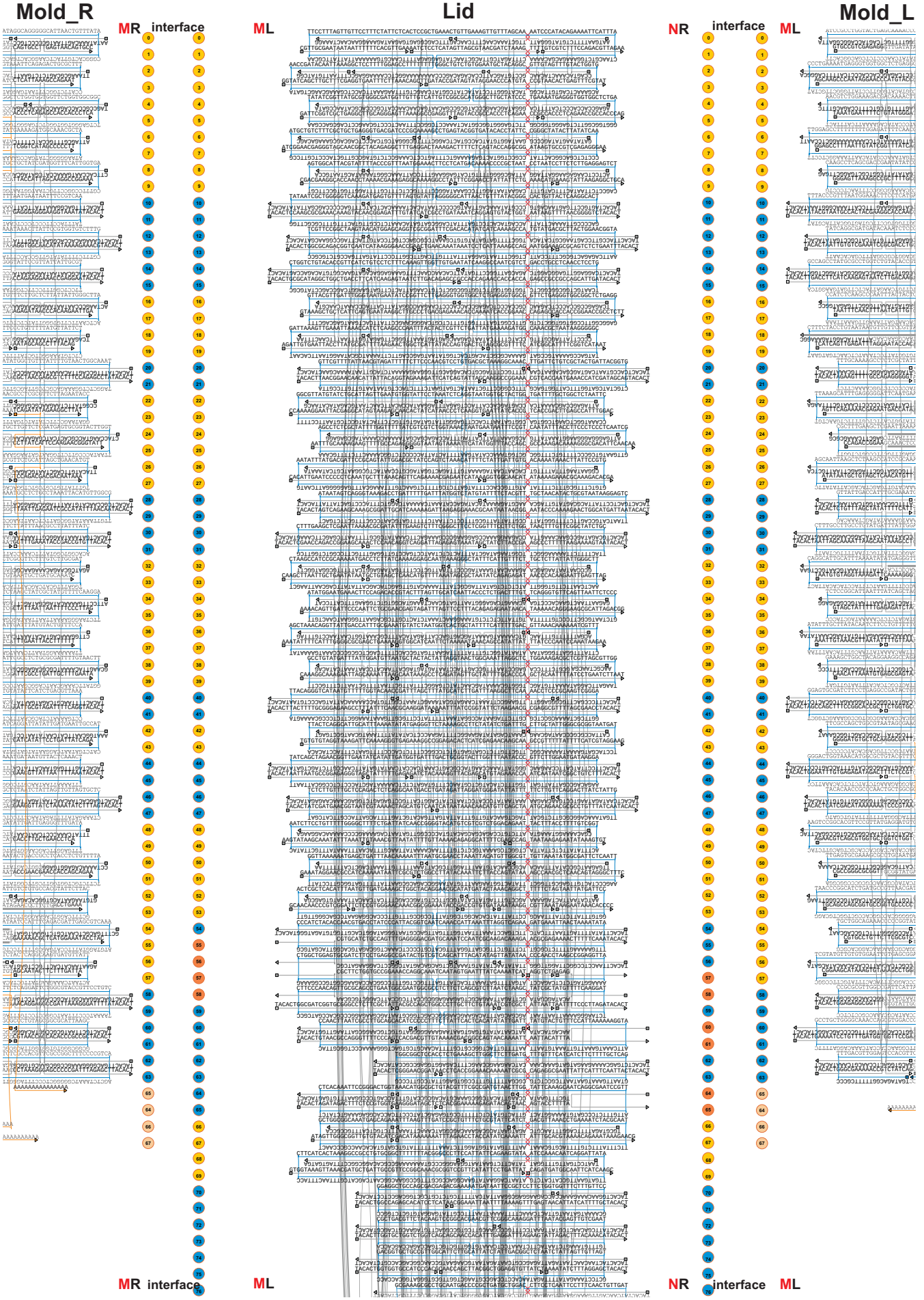
Mold_R
MR
interface
Lid
ML
NR
interface
Mold_L
ML
MR
interface
ML
NR
interface
ML

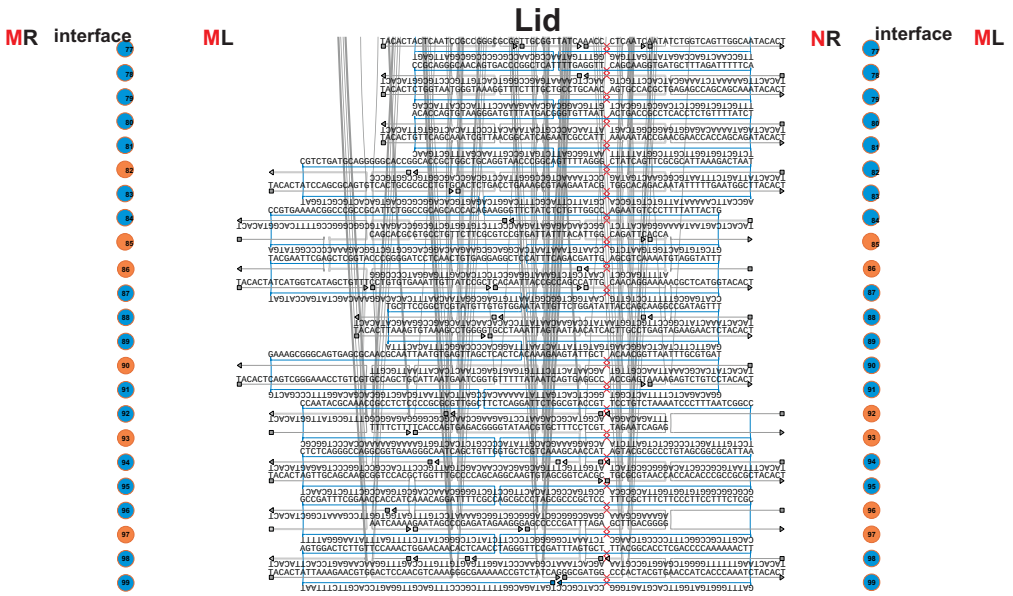

Figure S23. Design template of the *lid element* (center) with interfaces M and N to right and left *mold* ends.
Attractive helix ends have either 2 nt 5' staple extensions and 2 nt 3' staple recessions or vice versa. They are marked with yellow circles. Repulsive helix ends carry 5'-TACACT ssDNA extensions at the 5' and 3'-ends: They are marked with blue circles. 'Neutral ' helix ends ate which end staples were omitted are shown in orange. Colors and symbols are as in Figure S22.

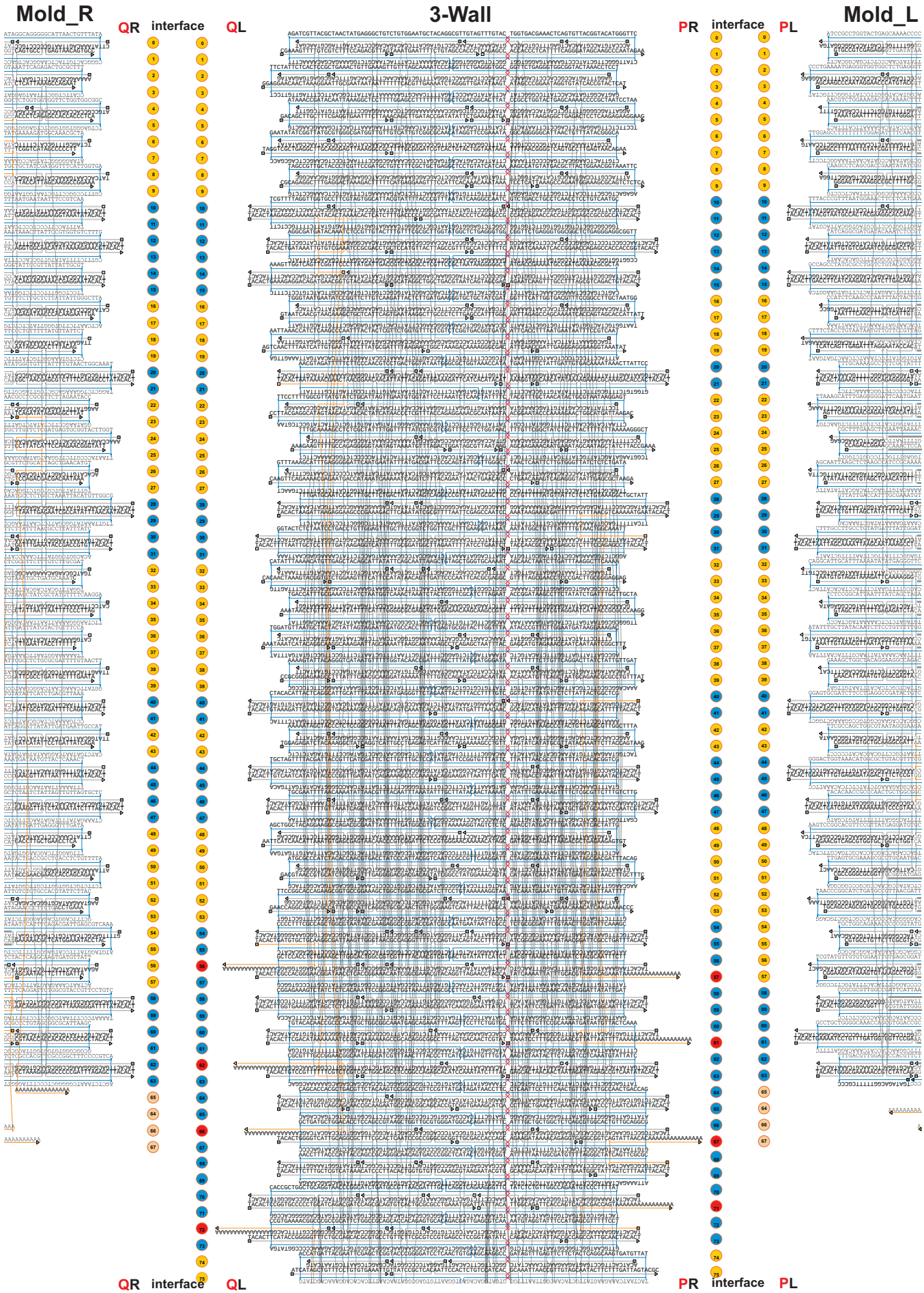
Mold_R
QR
interface
QL
3-Wall
PR
interface
PL
Mold_L
QR
interface
QL
PR
interface
PL

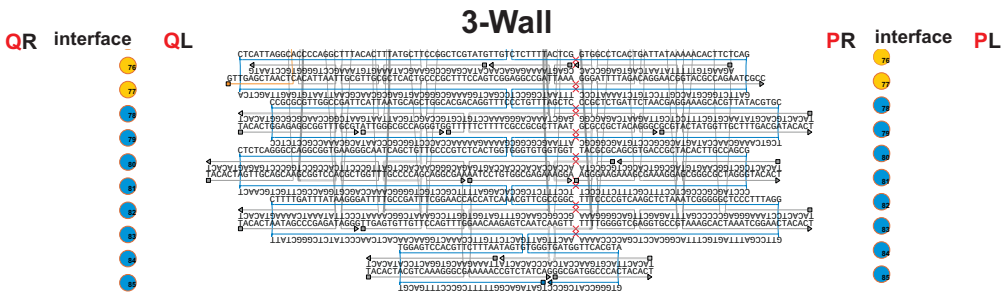

Figure S24. Design template of the *3-wall element* (center) with interfaces P and Q to left and right *mold* ends.
Attractive and repulsive helix ends are marked with yellow and blue circles respectively. Helix ends containing overhangs to capture DNA-coated AuNP seeds are marked with red circles. Staple overhangs, colors and symbols are as in Figure S22.

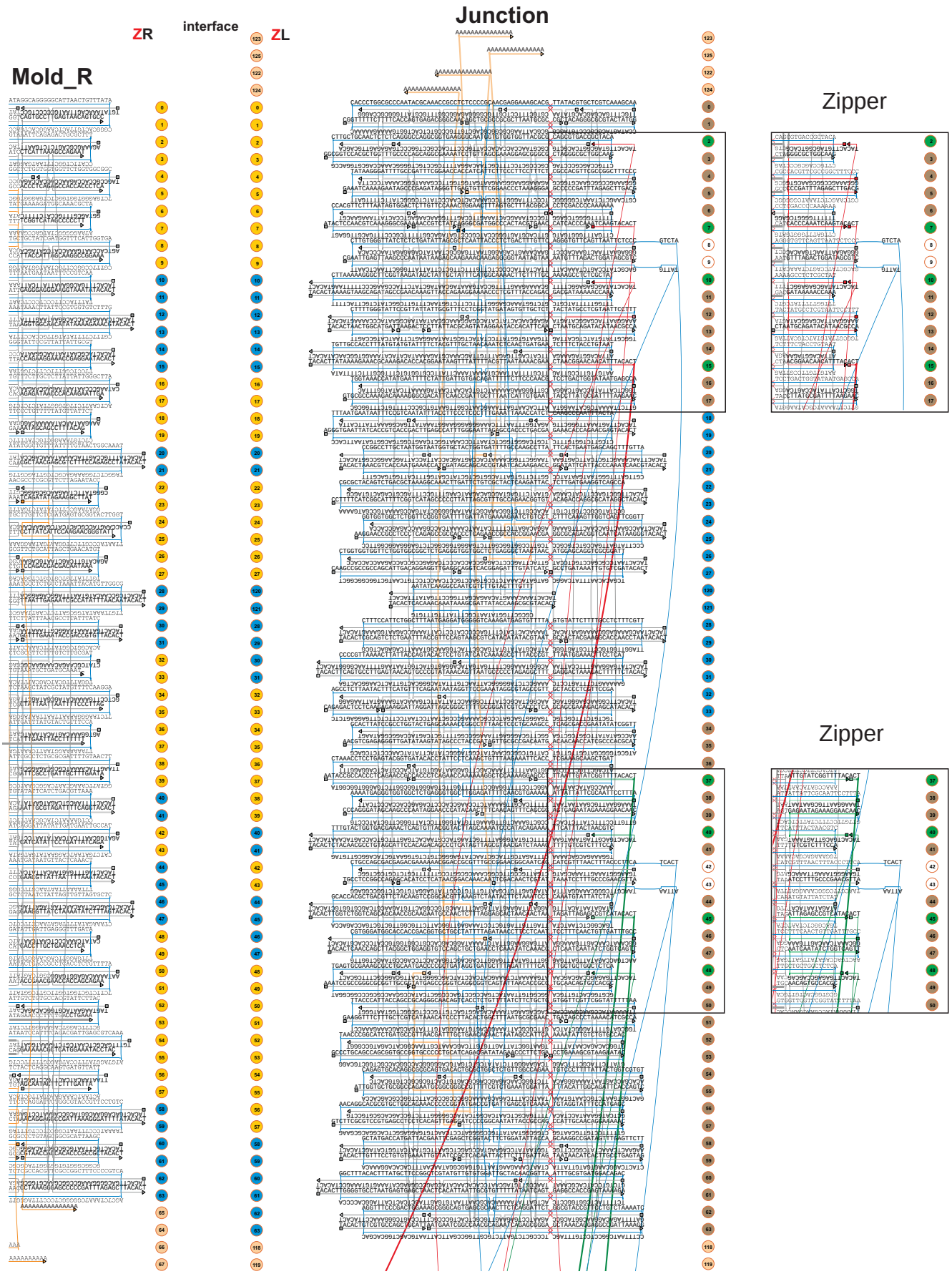
Junction
ZR
interface
ZL
Mold_R
Zipper
Zipper

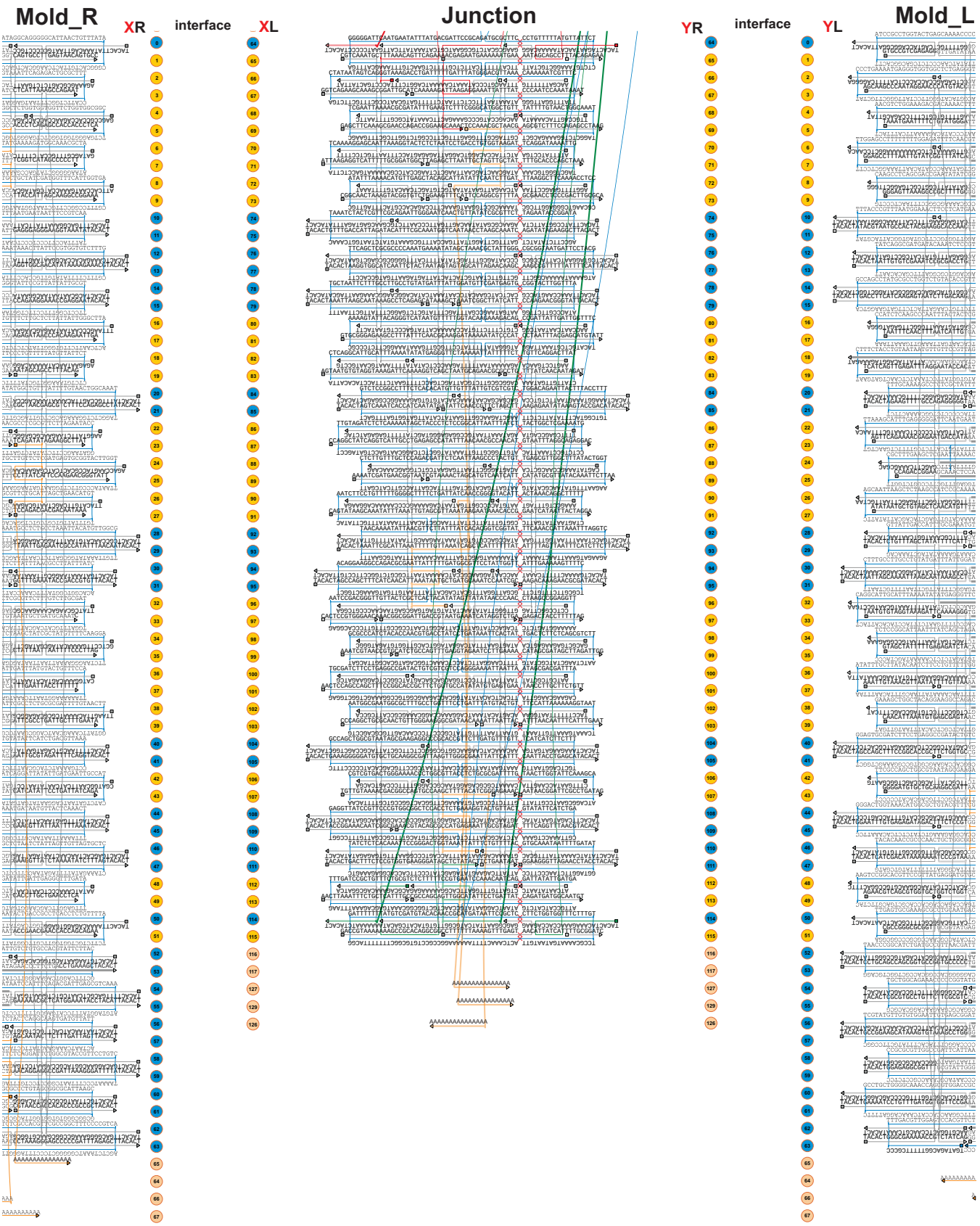

Figure S25. Design template of the *junction element* with interfaces X,Y and Z to *mold elements*. Drawn is the design of the junction element (center) together with a right mold end that docks via the Z interface to the bottom part of the junction as well as left and right mold ends that dock via the X and Y interfaces to the top part of the junction. Attractive, repulsive and blunt helix ends are marked with yellow, blue and brown circles respectively. Helix ends at which the scaffold or the connectors cross from the bottom to the top part are marked with white circles or green circles respectively. The main design shows connectors based on single staples, while the boxes on the right side show connectors based on the zipper geometry. For the latter the duplex part of the zipper strands is omitted. Their sequences are given for clarity in Figure S6. Staple overhangs, colors and symbols are as in Figure S22.

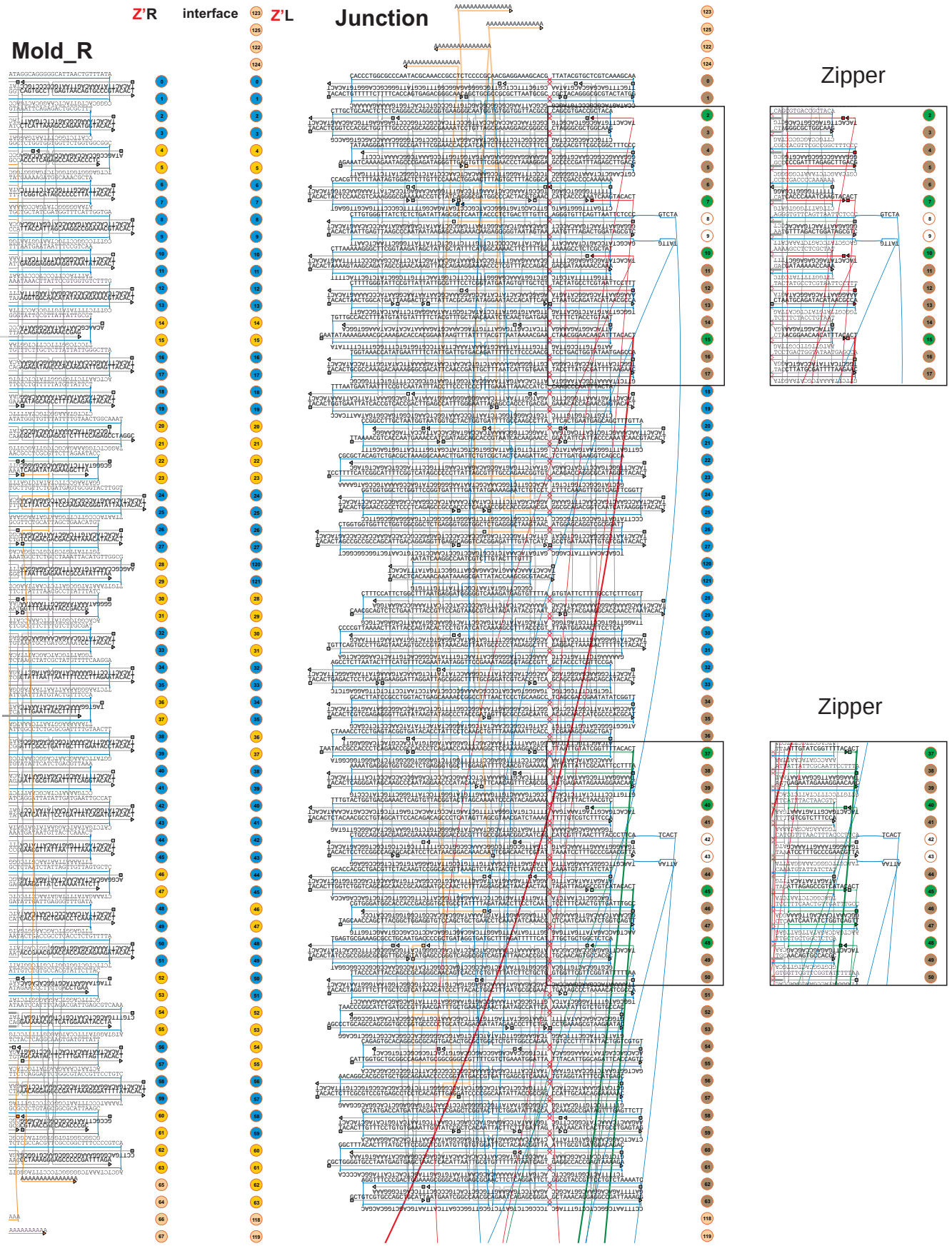

Figure S26. Design of the bottom part of the junction element (center) docking to a right mold end via the Z' interface.
For this interface staple extensions and recessions of 3 nt were used to form attractive ends. Colors and symbols are as in Figure S22.

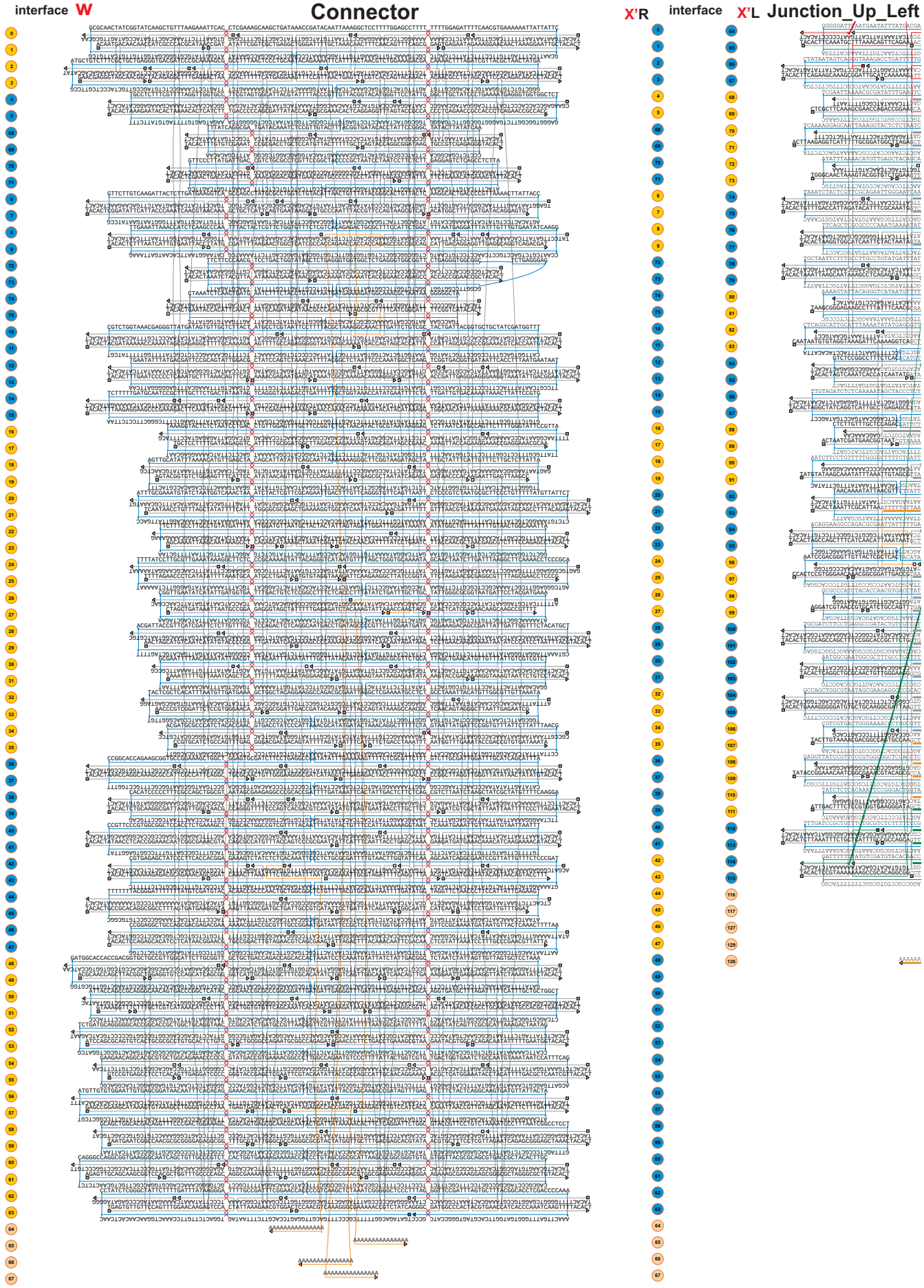

Figure S27. Design template of the *connector element* with the self-dimerizing interface W and the X' interface to the left end of the junction top part.
Attractive helices have either 5' end extensions and 3' end recessions of 3 nt or vice versa. Colors and symbols are as in Figure S22.

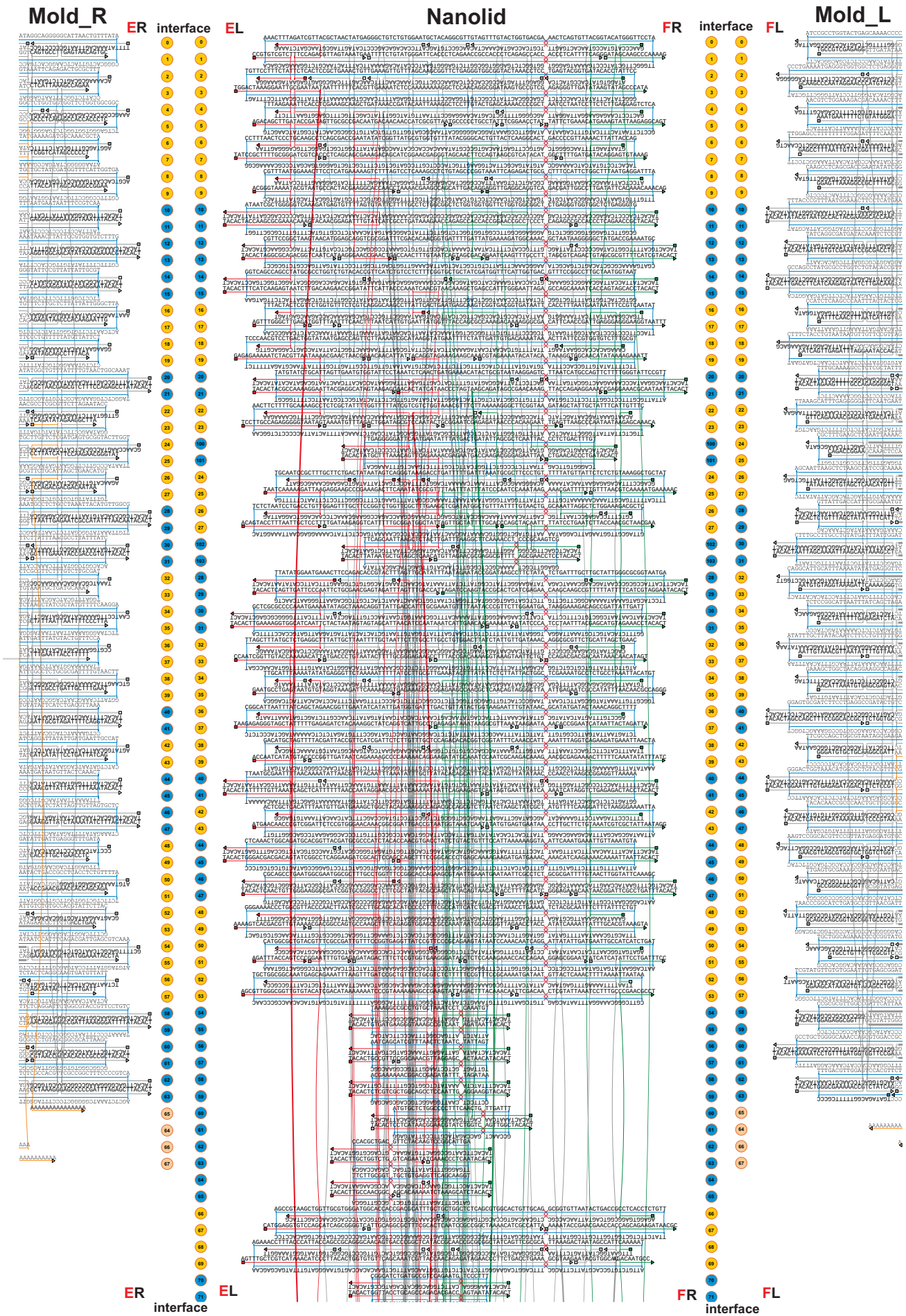
Mold_R
ER
interface
EL
Nanolid
FR
interface
FL
Mold_L
ER
interface
EL
FR
interface
FL

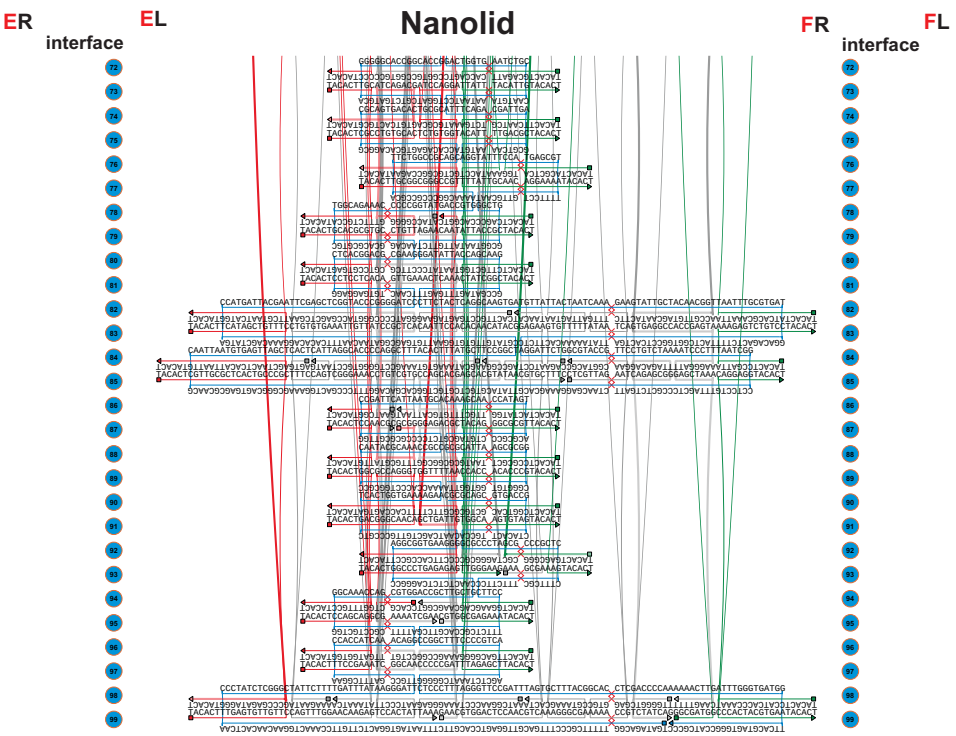

Figure S28. Design template of the *nanolid element* (center) with interfaces F and E to left and right *mold* ends.
Attractive and repulsive helix ends are marked with yellow and blue circles respectively. Staple overhangs, colors and symbols are as in Figure 22.

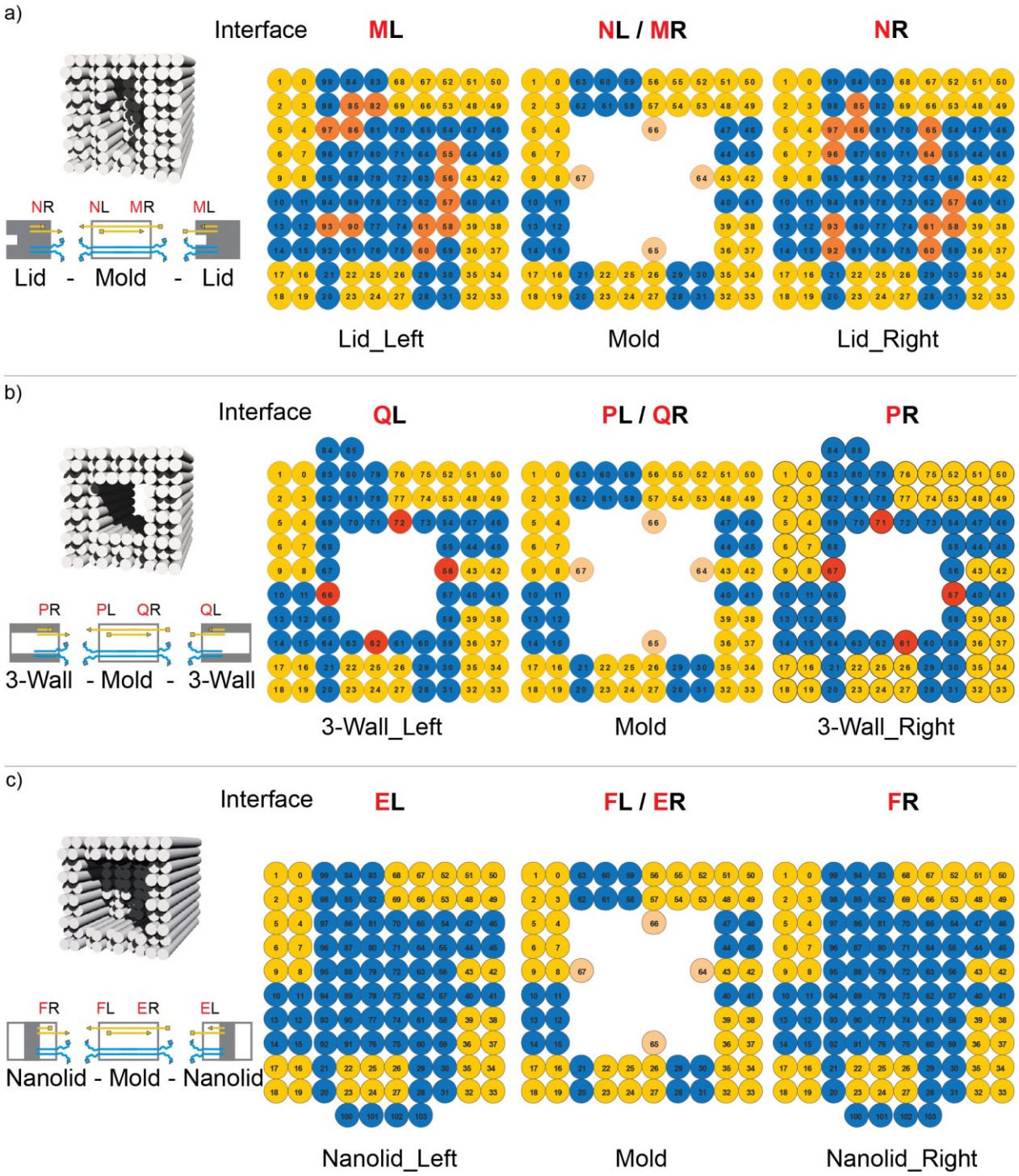

Figure S29. Summary of the interface designs for lid-mold and 3-wall-mold interactions. Colors at the helix ends indicate attractive (in yellow), repulsive (in blue), 'neutral' ends (in orange) and AuNP capture ends (in red). (**a**) N interface for the docking of a right lid end to a left mold end as well as the M interface for the docking of a left lid end to a right mold end. (**b**) P interface for the docking of a right end of a 3-wall mold to a left mold end as well as the Q interface for the docking of a left end of a 3-wall mold to a right mold end. (**c**) F interface for the docking of a right end of a nanolid to a left mold end as well as the E interface for the docking of a left end of a nanolid to a right mold end.

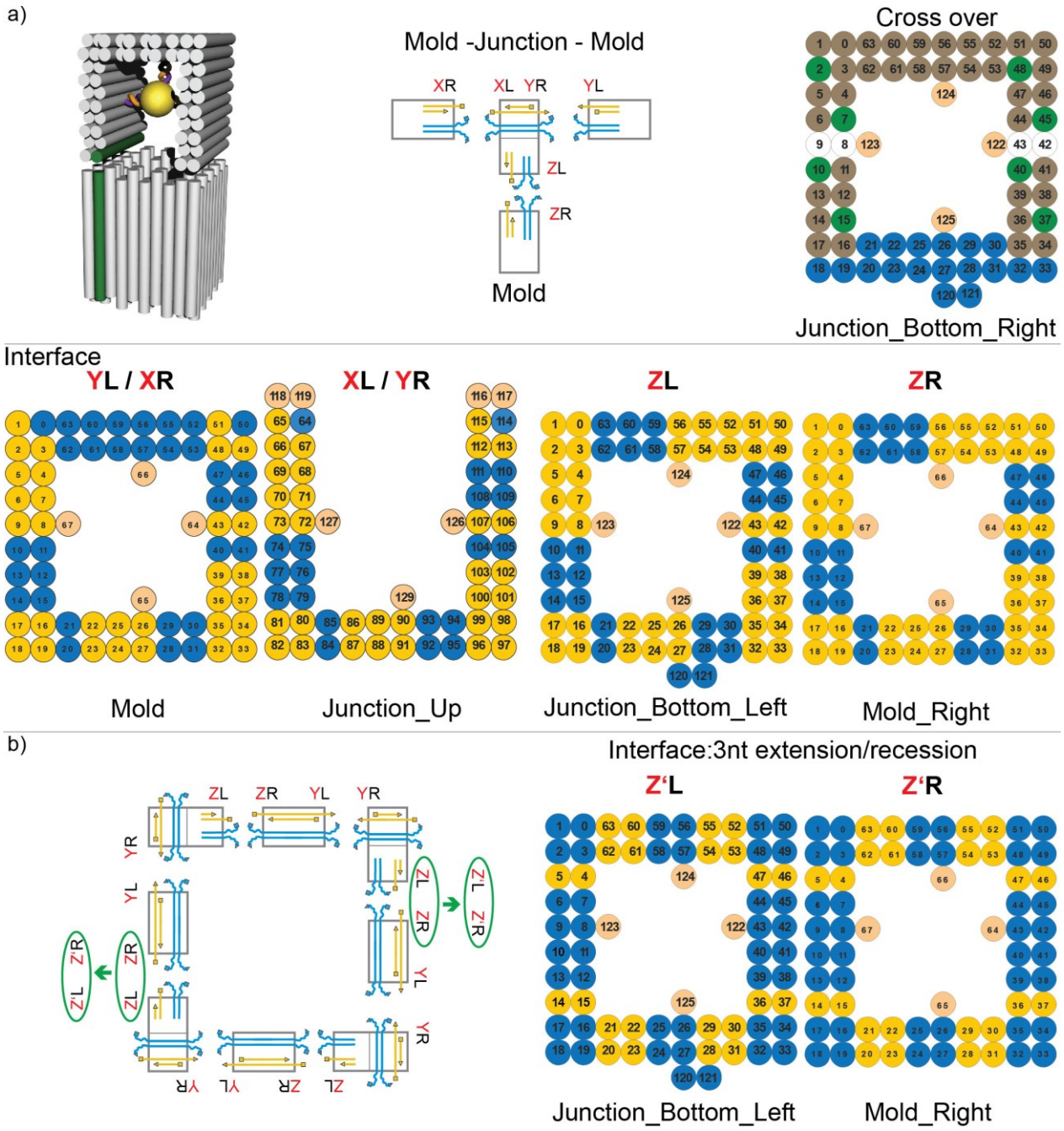

Figure S30. Summary of the interface design for junction-mold interactions.
(**a**) The junction element can bind three individual molds. Top row: 3D scheme of the junction element (left); location of the X, Y and Z interfaces to allow mold binding by the junction (center); location of connectors connect the top and the bottom part of the junction (right). Positions of staple connectors are shown in green; positions of scaffold crossovers are shown in white; blunt DNA ends are shown in brown; DNA ends with single stranded overhangs are shown in blue. Bottom row: Design of X, Y and Z interfaces for junction-mold docking. Colors at the helix ends indicate attractive (in yellow) and repulsive (in blue) ends. (**b**) Left: Location of the Z' variant (indicated by green circles) of the Z interface within a square loop structure. Due to less attractive helix ends and 3 nt extensions/recessions at the end staples it provides a lower affinity compared to the Z interface. Color codes are as in Figure S29.

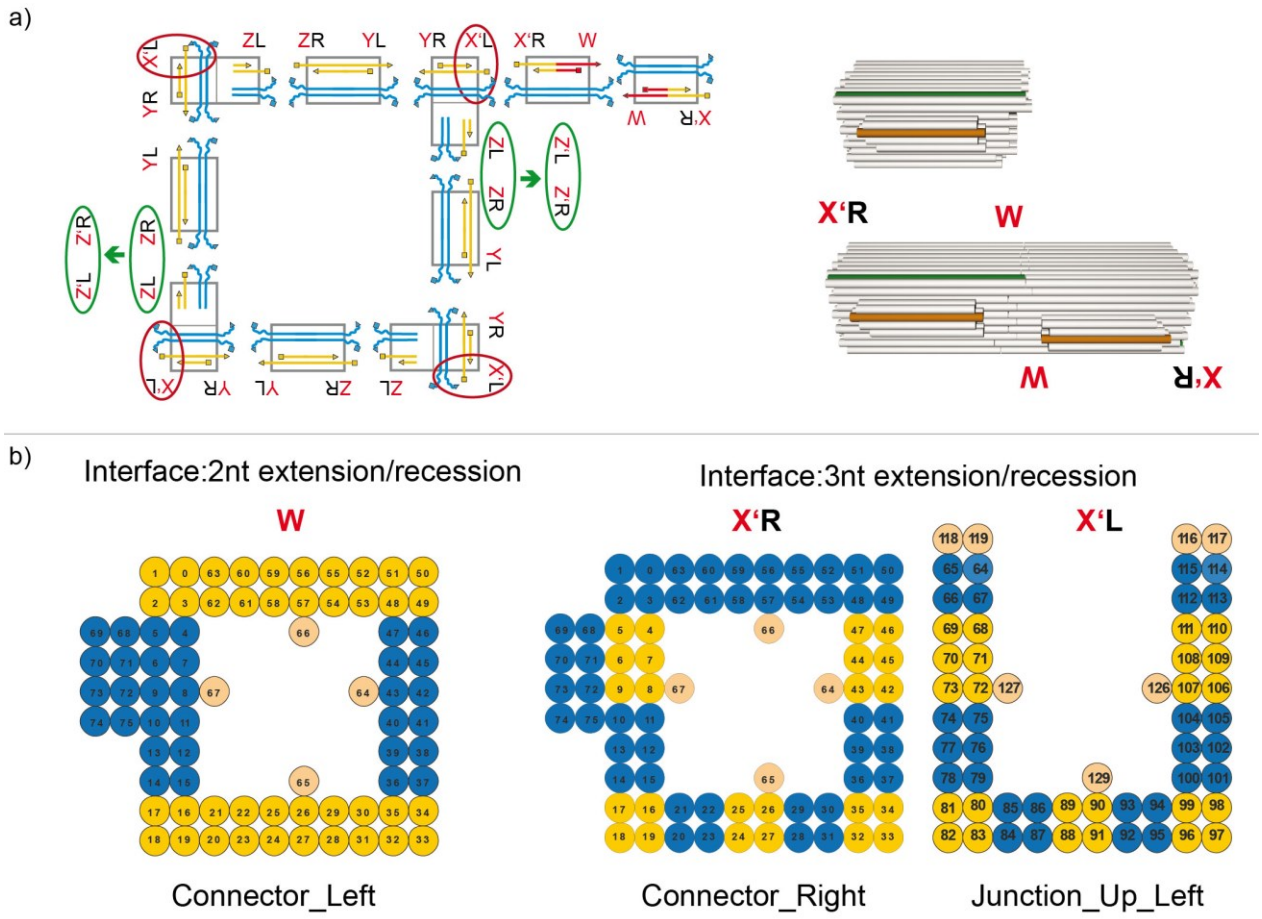

Figure S31. Summary of the interface design for network formation.
(**a**) Left: scheme of the interface locations for network formation including the Y, Z interfaces of the square loop, the W interface for connector dimerization and the X' interface for connector-square loop interaction. Right: 3D model of the connector dimer. (**b**) Designs of the W interface for connector dimerization and the X' interface for connector square-loop interaction. Interface X' uses end staple extensions/recessions of 3 nt. Colors at the helix ends indicate attractive (in yellow) and repulsive (in blue) ends.

References

[1] T. Bayrak, S. Helmi, J. Ye, D. Kauert, J. Kelling, T. Schönherr, R. Weichelt, A. Erbe, R. Seidel, *Nano Lett.* **2018**, *18*, 2116.
[2] J. Ye, S. Helmi, J. Teske, R. Seidel, *Nano Lett.* **2019**, *19*, 2707.
[3] D.-N. Kim, F. Kilchherr, H. Dietz, M. Bathe, *Nucleic Acids Res.* **2012**, *40*, 2862.
[4] P. B. Johnson, R. W. Christy, *Phys. Rev. B* **1972**, *6*, 4370.
[5] M. Tebbe, C. Kuttner, M. Mayer, M. Maennel, N. Pazos-Perez, T. A. F. König, A. Fery, *J. Phys. Chem. C* **2015**, *119*, 9513.
[6] S. M. Douglas, A. H. Marblestone, S. Teerapittayanon, A. Vazquez, G. M. Church, W. M. Shih, *Nucleic Acids Research* **2009**, *37*, 5001.